

IS STRONG SASI ACTIVITY THE KEY TO SUCCESSFUL NEUTRINO-DRIVEN SUPERNOVA EXPLOSIONS?

FLORIAN HANKE, ANDREAS MAREK, BERNHARD MÜLLER, AND HANS-THOMAS JANKA

Max-Planck-Institut für Astrophysik, Karl-Schwarzschild-Str. 1, D-85748 Garching, Germany; fhanke@mpa-garching.mpg.de, thj@mpa-garching.mpg.de
Draft version July 25, 2018

ABSTRACT

Following a simulation approach of recent publications we explore the viability of the neutrino-heating explosion mechanism in dependence on the spatial dimension. Our results disagree with previous findings. While we also observe that two-dimensional (2D) models explode for lower driving neutrino luminosity than spherically symmetric (1D) models, we do not find that explosions in 3D occur easier and earlier than in 2D. Moreover, we find that the average entropy of matter in the gain layer hardly depends on the dimension and thus is no good diagnostic quantity for the readiness to explode. Instead, mass, integrated entropy, total neutrino-heating rate, and nonradial kinetic energy in the gain layer are higher when models are closer to explosion. Coherent, large-scale mass motions as typically associated with the standing accretion-shock instability (SASI) are observed to be supportive for explosions because they drive strong shock expansion and thus enlarge the gain layer. While 2D models with better angular resolution explode clearly more easily, the opposite trend is seen in 3D. We interpret this as a consequence of the turbulent energy cascade, which transports energy from small to large spatial scales in 2D, thus fostering SASI activity. In contrast, the energy flow in 3D is in the opposite direction, feeding fragmentation and vortex motions on smaller scales and thus making the 3D evolution with finer grid resolution more similar to 1D. More favorable conditions for explosions in 3D may therefore be tightly linked to efficient growth of low-order SASI modes including nonaxisymmetric ones.

Subject headings: supernovae: general — hydrodynamics — stars: interiors — neutrino

1. INTRODUCTION

Recent simulations in two dimensions (2D) with sophisticated neutrino transport have demonstrated that the neutrino-driven mechanism, supported by hydrodynamic instabilities in the postshock layer, can yield supernova explosions at least for some progenitor stars (11.2 and 15 M_{\odot} ones in Marek & Janka 2009; Müller et al. 2012). The explosions occur relatively late after bounce and tend to have fairly low energy, being “marginal” or only slightly above the “critical threshold” in this sense. Suwa et al. (2010) obtained a similar explosion for a 13 M_{\odot} progenitor in their axisymmetric simulations. However, the Oak Ridge group has found stronger and earlier explosions for a wider range of progenitors (Bruenn et al. 2009), while in purely Newtonian simulations with multi-dimensional neutrino diffusion (including energy dependence but without energy-bin coupling) Burrows et al. (2006, 2007) could not see any success of the delayed neutrino-driven mechanism.

While the reason for the discrepant results of these simulations cannot be satisfactorily understood on the basis of published results, the marginality of the 2D explosions of the Garching group and the lack of neutrino-driven explosions in the simulations by Burrows et al. (2006, 2007) raises the important question about the influence of the third spatial dimension on the post-bounce evolution of collapsing stellar cores. Three-dimensional (3D) fluid dynamics with their inverse turbulent energy cascade compared to the 2D case are likely to change the flow pattern on large scales as well as small scales. They could have an influence on the existence and the growth rate of nonradial hydrodynamic instabilities in the supernova core even in the absence of stellar rotation (see, e.g., Iwakami et al. 2008) but in particular with a moderate amount of angular momentum in the progenitor star (e.g., Blondin & Mezzacappa 2006a; Iwakami et al. 2009; Fernández 2010), and thus could lead to differences

in the hydrodynamic and thermodynamic conditions for the operation of the neutrino-heating mechanism. In particular, 3D flows might cause important changes of the dwell time of postshock matter in the layer where neutrinos deposit energy, which is a crucial aspect deciding about the viability and efficiency of the neutrino-driven supernova mechanism (some aspects of this were discussed by Murphy & Burrows 2008 and Marek & Janka 2009).

Indeed, employing a simplified treatment of neutrino effects by including local neutrino-cooling and heating terms for a chosen value of the neutrino luminosity and spectral temperature instead of solving the computationally intense neutrino transport, Nordhaus et al. (2010) found considerably easier and earlier explosions in 3D than in 2D. In the context of the concept of a critical value of the neutrino luminosity that (for a given mass accretion rate onto the stalled supernova shock) has to be exceeded to obtain neutrino-driven explosions (Burrows & Goshy 1993; Janka & Müller 1996; Janka 2001; Yamasaki & Yamada 2005; Murphy & Burrows 2008; Pejcha & Thompson 2011; Fernández 2012), they quantified the improvement of 3D relative to 2D by a 15–25% reduction of the critical luminosity value. In particular, they observed that 3D postshock convection leads to higher average entropies in the neutrino-heating layer, thus improving the conditions for shock revival due to a significant stretching of the residence time of matter in the layer where it gains energy from neutrinos. Very recently, Takiwaki et al. (2011) reported enhanced maximum dwell times of a small fraction of the material in the gain region in a 3D simulation compared to the 2D case of an 11.2 M_{\odot} star, but could not unambiguously link this effect to an easier explosion of the 3D model. In particular, their 3D simulation showed a shock expansion that was more delayed than in the 2D run, and the 3D conditions did not appear more favorable for an explosion with respect to a variety of quantities like the net heating rate, the heating timescale or the profiles of maximum and minimum entropies.

In this paper we present a comparative investigation for $11.2 M_{\odot}$ and $15 M_{\odot}$ progenitors in one, two, and three dimensions along the lines of the study by Nordhaus et al. (2010), varying the driving neutrino luminosities used in time-dependent collapse simulations of the two stars. While our results for spherically symmetric (1D) and 2D models basically confirm the dimension-dependent differences found by Murphy & Burrows (2008) and Nordhaus et al. (2010), our calculations do neither exhibit a strict 1D-2D-3D hierarchy of the average entropy in the gain layer, nor do they show any clear signs that 3D effects facilitate the development of the explosion better than nonradial motions in 2D. Attempting to understand the reason for this puzzling finding we vary the resolution of the spherical coordinate grid used for our 2D and 3D simulations. The outcome of these studies reflects the action of the energy flow within the turbulent energy cascade. The latter transports the driving energy provided by neutrino heating and gravitational energy release in the accretion flow from small to large scales in 2D and opposite in 3D. Models in 2D show growing large-scale asymmetry and quasi-periodic time variability and explode clearly easier with higher resolution, whereas in 3D better resolved models are observed to become more similar to the 1D case and thus to be farther away from an explosion. This suggests that the success of the neutrino-driven mechanism could be tightly linked to the initiation of strong non-radial mass motions in the neutrino-heated postshock layer on the largest possible scales, implying that the easier explosions of our 2D models with higher resolution are a consequence of more violent activity due to the standing accretion-shock instability (SASI; Blondin et al. 2003), whereas the better resolved 3D models for the employed artificial setup of supernova-core conditions tend to reveal considerably reduced amplitudes of low-order spherical-harmonics modes of nonradial deformation and thus behave more similar to the 1D case.

The paper is structured as follows. In Sect. 2 we briefly describe our numerics and implementation of neutrino source terms. In Sect. 3 we give an overview of the simulations presented in this paper. Our investigations of the dependence of the critical luminosity on the spatial dimension will be presented in Sect. 4 and results of resolution studies in Sect. 5. An interpretation of our findings will follow in Sect. 6. Section 7 contains the summary and conclusions. In App. A we present 1D simulations that document our efforts to reproduce the results of previous, similar studies in the literature by straightforwardly applying the neutrino treatment described in these works.

2. NUMERICAL SETUP

We solve the equations of hydrodynamics reflecting the conservation of mass, momentum, and energy,

$$\frac{\partial \rho}{\partial t} + \nabla \cdot (\rho \mathbf{v}) = 0, \quad (1)$$

$$\frac{\partial \rho \mathbf{v}}{\partial t} + \nabla \cdot (\rho \mathbf{v} \otimes \mathbf{v}) + \nabla P = -\rho \nabla \Phi, \quad (2)$$

$$\frac{\partial e}{\partial t} + \nabla \cdot [(e + P) \mathbf{v}] = -\rho \mathbf{v} \cdot \nabla \Phi + \rho (Q_{\nu}^{+} - Q_{\nu}^{-}), \quad (3)$$

where ρ is the mass density, \mathbf{v} the fluid velocity, Φ the gravitational potential, P the pressure, and e the total (internal+kinetic) fluid energy density. These equations are integrated in a conservative form (for which reason the en-

ergy equation is solved for the total energy density) using the explicit, finite-volume, higher-order Eulerian, multi-fluid hydrodynamics code PROMETHEUS (Fryxell et al. 1991; Müller et al. 1991a,b). It is a direct implementation of the Piecewise Parabolic Method (PPM) of Colella & Woodward (1984) using the Riemann solver for real gases developed by Colella & Glaz (1985) and the directional splitting approach of Strang (1968) to treat the multi-dimensional problem. In order to prevent odd-even coupling (Quirk 1994) we switch from the original PPM method to the HLLE solver of Einfeldt (1988) in the vicinity of strong shocks. The advection of nuclear species is treated by the Consistent Multi-fluid Advection (CMA) scheme of Plewa & Müller (1999).

To facilitate comparison with Nordhaus et al. (2010) we also employ the high-density equation of state (EoS) of Shen et al. (1998) and do not include general relativistic corrections. We use the monopole approximation of the Poisson equation to treat Newtonian self-gravity.

To make our extensive parameter study possible, we use the local source terms applied by Murphy & Burrows (2008) and Nordhaus et al. (2010) instead of detailed neutrino transport (see Janka 2001 for a derivation of these source terms). In this approach the neutrino heating and cooling rates Q_{ν}^{+} and Q_{ν}^{-} are given by

$$Q_{\nu}^{+} = 1.544 \cdot 10^{20} \left(\frac{L_{\nu_e}}{10^{52} \text{ erg s}^{-1}} \right) \left(\frac{T_{\nu_e}}{4 \text{ MeV}} \right)^2 \quad (4)$$

$$\left(\frac{100 \text{ km}}{r} \right)^2 (Y_n + Y_p) e^{-\tau_{\text{eff}}} \left[\frac{\text{erg}}{\text{g s}} \right],$$

$$Q_{\nu}^{-} = 1.399 \cdot 10^{20} \left(\frac{T}{2 \text{ MeV}} \right)^6 (Y_n + Y_p) e^{-\tau_{\text{eff}}} \left[\frac{\text{erg}}{\text{g s}} \right]. \quad (5)$$

These approximations depend on local quantities, namely the density ρ , the temperature T , the distance from the center of the star r , and the neutron and proton number fractions Y_n and Y_p , respectively. In Eq. (4) the electron-neutrino luminosity L_{ν_e} is a parameter and is assumed to be equal to the electron antineutrino luminosity $L_{\bar{\nu}_e} = L_{\nu_e}$. The neutrino temperature T_{ν_e} is set to 4 MeV.

The employed source terms, Eqs. (4) and (5), without the factors $e^{-\tau_{\text{eff}}}$ are valid for optically thin regions only. In order to model the transition to neutrino trapping at high optical depths, we follow Nordhaus et al. (2010) and multiply the heating and cooling terms by $e^{-\tau_{\text{eff}}}$ to suppress them in the inner opaque core of the proto-neutron star. Here, the optical depth for electron neutrinos and antineutrinos is defined as

$$\tau_{\text{eff}}(r) = \int_r^{\infty} \kappa_{\text{eff}}(r') dr'. \quad (6)$$

The effective opacity κ_{eff} was derived by Janka (2001) and given in Murphy et al. (2009):

$$\kappa_{\text{eff}} \approx 1.5 \cdot 10^{-7} \cdot X_{n,p} \left(\frac{\rho}{10^{10} \text{ g cm}^{-3}} \right) \left(\frac{T_{\nu_e}}{4 \text{ MeV}} \right)^2 \text{ cm}^{-1}, \quad (7)$$

where $X_{n,p} = \frac{1}{2}(Y_n + Y_p)$ accounts for composition averaging. In multi-dimensional simulations we evaluate the radial integration for the optical depth τ_{eff} independently for each latitude θ in 2D and each pair of latitudinal and azimuthal angles (θ, ϕ) in 3D. Note that in Murphy & Burrows (2008) the exponential suppression factor is absent in the heating and cooling terms (or was not mentioned), which otherwise agree

with ours, while no definition of the effective optical depth τ_{eff} is given in Nordhaus et al. (2010). The factor $(Y_n + Y_p)$ in Eqs. (4) and (5) is included in Nordhaus et al. (2010), but not in Murphy & Burrows (2008) and Murphy et al. (2009).

The time period from the onset of the collapse until 15 ms after bounce was tracked with the PROMETHEUS-VERTEX code (Rampp & Janka 2002) in 1D including its detailed, multi-group neutrino transport, all relevant neutrino reactions and a “flashing treatment” for an approximative description of nuclear burning during infall. This means that until 15 ms after bounce we describe neutrino effects including the evolution of the electron fraction Y_e with high sophistication. At 15 ms after core bounce we switch to the simple neutrino heating and cooling terms and upon mapping from 1D to 2D also impose (on the whole computational grid) random zone-to-zone seed perturbations with an amplitude of 1% of the density to break spherical symmetry.

Although during the subsequent evolution we apply the heating and cooling expressions of Eqs. (4) and (5) following Nordhaus et al. (2010) and Murphy & Burrows (2008), we refrain from adopting their treatment of changes of the electron fraction Y_e . Following a suggestion by Liebendörfer (2005), they prescribed Y_e simply as a function of density, $Y_e(\rho)$, instead of solving a rate equation with source terms for electron neutrino and antineutrino production and destruction consistently with the expressions employed for neutrino heating and cooling. Liebendörfer (2005) found that such a parametrization, supplemented by a corresponding entropy source term (and a neutrino pressure term in the equation of motion), yields results in good agreement with 1D simulations including neutrino transport during the collapse phase until the moment of bounce-shock formation. A universal Y_e - ρ -relation, which serves as the basis of this approximation and can be inferred for the infalling matter during the homologous collapse phase, however, applies neither for the evolution of the shocked accretion flow in the post-bounce phase nor for expanding neutrino-heated gas (see, e.g., Fig. 4.9 in Thielemann et al. 2011). For example, a comparison with supernova models with detailed neutrino transport shows that the Y_e - ρ -relation fitted to the homologous phase overestimates the deleptonization of the gas in most of the gain layer but underestimates the lepton loss of matter in the cooling layer and neutrinospheric region. Moreover, the question arises how the lepton evolution shall be treated in matter that reexpands and thus moves from high to low density? Even more, the entropy source term introduced in Eq. (5) of Liebendörfer (2005) is designed to specifically account for gas-entropy changes due to neutrino production by electron captures and subsequent energy transfers in (neutrino-electron) scatterings. The corresponding energy loss or gain rate of the medium through the escape or capture of electron neutrinos with mean energy E_{ν_e} , which is given by $\delta Q_{\nu_e}/\delta t = E_{\nu_e} \delta Y_e/\delta t$, is not included in the heating and cooling terms Q_{ν}^+ and Q_{ν}^- of Eqs. (4,5) of the present work. Adding it as an extra term would imply partial double-counting of the energy exchange via electron neutrinos, and omitting it means to overestimate the entropy increase in infalling, deleptonizing matter and to underestimate entropy gains of decompressed gas with growing Y_e . Because of the long list of such inconsistencies, whose implications are hard to judge or control, we decided to ignore Y_e changes of the stellar medium in our post-bounce simulations (except for the models discussed in App. A).

This choice can be justified, but it is certainly not a perfect

approach because it may also exclude effects of importance in real supernova cores, whose physical processes require the inclusion of neutrino transport for an accurate description of the energy and lepton-number evolution. One of the undesired consequences of keeping Y_e fixed in the accretion flow after core bounce is an overestimation of the electron pressure in the gas settling onto the forming neutron star. In order to enforce more compression and thus to ensure close similarity of our results to the 1D models studied by Nordhaus et al. (2010) and Murphy & Burrows (2008), we have to enhance the net cooling of the accreted matter by reducing the effective opacity κ_{eff} by a factor of 2.7 compared to the value given in Murphy et al. (2009) and in Eq. (7). This reduction factor is chosen such that our simulations reproduce the minimum values of the critical luminosity found to be necessary for triggering explosions of the $15 M_{\odot}$ progenitor ($2.6 \cdot 10^{52} \text{ erg s}^{-1}$) and for the $11.2 M_{\odot}$ star ($1.3 \cdot 10^{52} \text{ erg s}^{-1}$) in the 1D simulations of Murphy & Burrows (2008). Without the reduction factor of κ_{eff} , our models turn out to explode too easily because of weak cooling (see the results in App. A). We stress that any exponential suppression factor of the heating and cooling rates in Eqs. (4,5) is a pragmatic and ad hoc procedure to bridge the transition from the optically thin to the optically thick regime, where neutrino transport is most complicated. From transport theory neither the exponential factor nor the exact definition of the optical depth of the exponent can be rigorously derived.

In our reference set of standard simulations, we employ 400 non-equidistant radial zones, which are distributed from the center to an outer boundary at 9000 km. The latter is sufficiently far out to ensure that the gas there remains at rest during the simulated evolution periods. The radial zones are chosen such that the resolution $\Delta r/r$ is typically better than 2%. In the multi-dimensional models with standard resolution, we employ a polar grid with an angular bin size of 3° (60 θ - and 120 ϕ -zones). For the high-resolution 1D and multi-dimensional models of Sects. 4 and 5 we compute with up to 800 radial zones and in 2D with an angular resolution down to 0.5° , in 3D down to 1.5° . The additional radial grid zones are distributed such that the region between 20 and 400 km, i.e., not only the cooling layer around the neutrinosphere but also the gain layer between gain radius and shock, are resolved significantly better. While full convergence of the 1D results requires 600 radial zones or more, most of the plots comparing models for different dimensions show simulations with our standard resolution of only 400 radial cells (unless stated otherwise), because this is the limit for which we could perform a larger set of 3D runs in acceptable time. To avoid an extremely restrictive Courant-Friedrich-Lewy (CFL) timestep in our 3D calculations, we simulate the inner core above a density of $\rho = 10^{12} \text{ g/cm}^3$ in spherical symmetry.

3. INVESTIGATED PROGENITORS AND MODELS

Our models are based on the $15 M_{\odot}$ progenitor star s15s7b2 of Woosley & Weaver (1995) and an $11.2 M_{\odot}$ progenitor of Woosley et al. (2002). The calculations for these progenitors with our standard angular resolution of 3° are summarized in Table 1. This table is arranged such that horizontal rows have the same driving luminosities for simulations performed in different dimensions. Varying the prescribed driving luminosity L_{ν_e} from run to run we present for each of the $11.2 M_{\odot}$ and $15 M_{\odot}$ progenitors several 1D, 2D, and 3D simulations. All of the 1D and 2D simulations cover at least 1s after bounce. The nonexploding 3D simulations with standard angular resolution of 3 degrees were not stopped until at least 600 ms af-

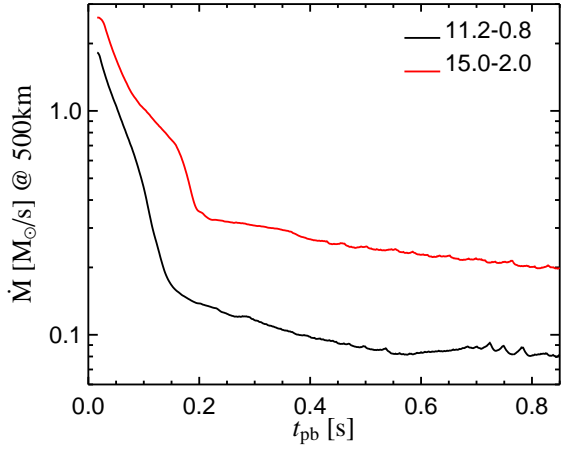


FIG. 1.— Time evolution of the mass accretion rate, $\dot{M}(r) = 4\pi r^2 \rho(r) |v(r)|$, evaluated at 500 km for the $11.2 M_\odot$ and the $15 M_\odot$ progenitors in nonexploding models.

TABLE 1
11.2 M_\odot AND 15 M_\odot RESULTS WITH STANDARD GRID OF 400 RADIAL ZONES AND 3 DEGREES ANGULAR RESOLUTION.

$L_{\nu_e}^a$ (10^{52} erg/s)	1D		2D		3D	
	t_{exp}^b (ms)	\dot{M}_{exp}^c (M_\odot/s)	t_{exp} (ms)	\dot{M}_{exp} (M_\odot/s)	t_{exp} (ms)	\dot{M}_{exp} (M_\odot/s)
11.2 M_\odot						
0.8	—	—	—	—	—	—
0.9	—	—	—	—	731	0.085
1.0	—	—	563	0.082	537	0.086
1.1	—	—	461	0.091	—	—
1.2	—	—	357	0.104	319	0.112
1.3	819	0.082	307	0.114	—	—
1.4	499	0.088	241	0.126	232	0.130
1.5	380	0.100	232	0.130	—	—
1.6	345	0.106	203	0.137	—	—
15 M_\odot						
2.0	—	—	—	—	—	—
2.1	—	—	—	—	—	—
2.2	—	—	876	0.197	612	0.226
2.3	—	—	428	0.261	426	0.261
2.4	—	—	442	0.255	—	—
2.5	—	—	283	0.313	281	0.314
2.6	710	0.215	285	0.312	—	—
2.7	489	0.247	262	0.316	—	—
2.8	390	0.271	242	0.322	236	0.324
2.9	281	0.314	235	0.325	—	—
3.0	258	0.318	236	0.324	—	—
3.1	248	0.320	220	0.327	—	—

^a Electron-neutrino luminosity.

^b Time after bounce of onset of explosion. A “—” symbol indicates that the model does not explode during the simulated period of evolution.

^c Mass accretion rate at onset of explosion.

ter bounce. For models with higher resolution the simulation times are given in Table 2.

In Table 1 the time of the onset of an explosion, t_{exp} , and the mass accretion rate at that time, \dot{M}_{exp} , are listed as characteristic quantities of the models. The beginning of the explosion is defined as the moment of time t_{exp} when the shock reaches an average radius of 400 km (and does not return later on), while nonexploding models are denoted by a “—” symbol. In multidimensional simulations the corresponding shock position is defined as the surface average over all angular directions, $\langle R_S \rangle \equiv \frac{1}{4\pi} \oint d\Omega R_S(\vec{\Omega})$. The lowest driving luminosity

yielding an explosion for a given value of the mass accretion rate is termed the critical luminosity (Burrows & Goshy 1993; Murphy & Burrows 2008). We determine the mass accretion rate $\dot{M}(r) = 4\pi r^2 \rho(r) |v(r)|$ at the time of the onset of the explosion just exterior to the shock, i.e. at a radius of 500 km, where the infalling envelope is spherical (except for the small seed perturbations imposed on the multi-dimensional models). In Fig. 1 the mass accretion rates of the $11.2 M_\odot$ and $15 M_\odot$ progenitors are depicted for the nonexploding runs with the lowest driving neutrino luminosities. Because the shock can be largely deformed in multi-dimensional simulations and its outermost parts can extend beyond 500 km (and thus impede a clean determination of the mass accretion rate) when its average radius just begins to exceed 400 km, we refer to the functions plotted in Fig. 1 for defining the mass accretion rate at the time when the explosion sets in.

4. CRITICAL LUMINOSITY AS FUNCTION OF DIMENSION

Based on steady-state solutions of neutrino-heated and -cooled accretion flows between the stalled shock and the proto-neutron star surface, Burrows & Goshy (1993) identified a critical condition that can be considered to separate exploding from nonexploding models. They found that for a given value of the mass infall rate \dot{M} onto the accretion shock steady-state solutions cannot exist when the neutrino-heating rate in the gain layer is sufficiently large, i.e., for neutrino luminosities above a threshold value L_ν . This result can be coined in terms of a critical condition $L_\nu(\dot{M})$ expressing the fact that either the driving luminosity has to be sufficiently high or the damping mass accretion rate enough low for an explosion to become possible. The critical \dot{M} - L_ν -curve was interpreted by Burrows & Goshy (1993) as a separating line between the region above, where due to the non-existence of steady-state accretion solutions explosions are expected to take place, from the region below, where neutrino energy input behind the shock is insufficient to accelerate the stalled shock outwards and thus to trigger an explosion.

This interpretation of the steady-state results was consistent with hydrodynamical simulations of collapsing and exploding stars in 1D and 2D by Janka & Müller (1996). Performing a more extended parameter study than the latter work, Murphy & Burrows (2008) explored the concept of a critical condition systematically with time-dependent hydrodynamical models. They showed that a critical luminosity indeed separates explosion from accretion and confirmed that this value is lowered by $\sim 30\%$ when going from spherical symmetry to two dimensions, at least when a fixed driving luminosity is adopted and feedback effects of the hydrodynamics on the neutrino emission are ignored. Some 2D effects including possible consequences of rotation were discussed before on grounds of steady-state models by Yamasaki & Yamada (2005, 2006), while Janka (2001) tried to include time-dependent aspects of the shock-revival problem and took into account an accretion component of the neutrino luminosity in addition to the fixed core component. The influence of such an accretion contribution was more recently also estimated by Pejcha & Thompson (2011), who solved the one-dimensional steady-state accretion problem between the neutron star and the accretion shock along the lines of Burrows & Goshy (1993), but attempted to obtain a deeper understanding of the critical condition by comprehensively analysing the structure of the accretion layer and of the limiting steady-state solution in dependence of the stellar conditions. They found that the critical value for the neutrino lumi-

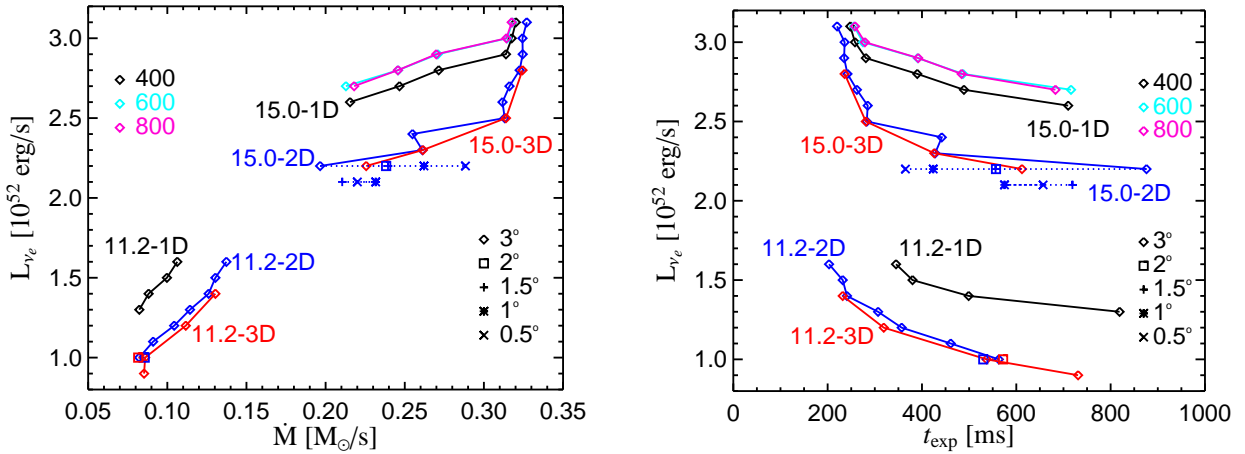


FIG. 2.— Critical curves for the electron-neutrino luminosity (L_{ν_e}) versus mass accretion rate (\dot{M}) (left plot) and versus explosion time t_{exp} (right plot) for simulations in 1D (black), 2D (blue), and 3D (red) with standard resolution. The accretion rate is measured just outside of the shock at the time t_{exp} when the explosion sets in. For the 15 M_{\odot} progenitor 1D results are displayed for 400, 600, and 800 radial zones. Higher radial resolution compared to the standard 1D runs makes explosions slightly more difficult; convergence is achieved for ≥ 600 radial bins. Multi-dimensional results are shown for different angular resolutions, where available, but always computed with 400 radial zones. Note that 2D simulations with improved angular zoning explode more easily, whereas in 3D only one case was computed (the 11.2 M_{\odot} simulation for $L_{\nu_e} = 1.0 \cdot 10^{52}$ erg s $^{-1}$) that developed an explosion also with better angular resolution.

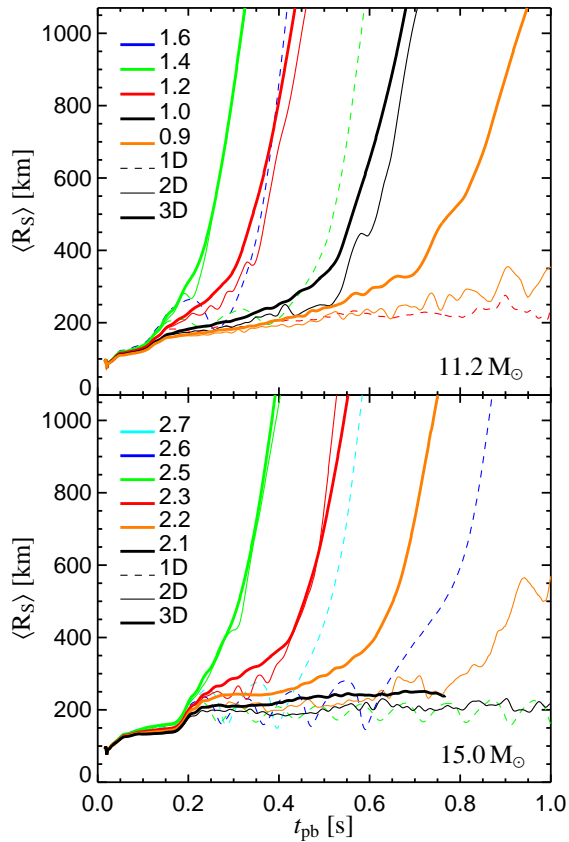


FIG. 3.— Time evolution of the average shock radius as function of the post-bounce time t_{pb} for simulations in one (thin dashed lines), two (thin solid lines), and three dimensions (thick lines). The shock position is defined as the surface average over all angular directions. The top panel shows results for the 11.2 M_{\odot} progenitor and the bottom panel for the 15 M_{\odot} progenitor, all obtained with our standard resolution. Different electron-neutrino luminosities (labelled in the plots in units of 10^{52} erg s $^{-1}$) are displayed by different colors.

osity is linked to an “antesonic condition” in which the ratio of the adiabatic sound speed to the local escape velocity in the postshock layer reaches a critical value above which steady-state solutions of neutrino-heated accretion flows cannot be obtained. By performing high-resolution hydrodynamic sim-

ulations Fernández (2012) found that radial instability is a sufficient condition for runaway expansion of an initially stalled core-collapse supernova shock if the neutrinospheric parameters do not vary with time and if heating by the accretion luminosity is neglected. However, the threshold neutrino luminosities for the transition to runaway instability are in general different from the limiting values for steady-state solutions of the kind discussed by Burrows & Goshy (1993) and Pejcha & Thompson (2011). Nordhaus et al. (2010) generalized the hydrodynamic investigations of Murphy & Burrows (2008) to include 3D models and found another reduction of the threshold luminosity for explosion by 15–25% compared to the 2D case.

Despite the basic agreement of the outcome of these investigations it should be kept in mind that it is not ultimately clear whether the simple concept of a critical threshold condition separating explosions from failures (and the dependences of this threshold on dimension and rotation for example) holds beyond the highly idealized setups considered in the mentioned works. None of the mentioned systematic studies by steady-state or hydrodynamic models was able to include adequately the complexity of the feedback between hydrodynamics and neutrino transport physics. In particular, none of these studies could yield the proof that the non-existence of a steady-state accretion solution for a given combination of mass accretion rate and neutrino luminosity is equivalent to the onset of an explosion. The latter requires the persistence of sufficiently strong energy input by neutrino heating for a sufficiently long period of time. This is especially important because Pejcha & Thompson (2011) showed that the total energy in the gain layer is still negative even in the case of the limiting accretion solution that corresponds to the critical luminosity¹. Within the framework of simplified modeling setups, however, the question cannot be answered whether such a persistent energy input can be maintained in the environment of the supernova core.

Following the previous investigations by Murphy & Burrows (2008) and Nordhaus et al. (2010) we performed hydrodynamical simulations that track the

¹ Note that Fernández (2012) demonstrated that transition to runaway occurs when the fluid in the gain region reaches positive specific energy.

post-bounce evolution of collapsing stars for different, fixed values of the driving neutrino luminosity. Since the mass accretion rate decreases with time according to the density profile that is characteristic of the initial structure of the progenitor core (see Fig. 1 for the 11.2 and $15 M_{\odot}$ stars considered in this work), each model run probes the critical value of \dot{M}_{exp} at which the explosion becomes possible for the chosen value of $L_{\nu} = L_{\nu_e} = L_{\bar{\nu}_e}$. The collection of value pairs $(\dot{M}_{\text{exp}}, L_{\nu_e})$ defines a critical curve $L_{\nu}(\dot{M})$. These are shown for our 1D, 2D, and 3D studies with standard resolution for both progenitor stars in the left panel of Fig. 2 and in the case of the $15 M_{\odot}$ star can be directly compared with Fig. 1 of Nordhaus et al. (2010). Table 1 lists, as a function of the chosen L_{ν_e} , the corresponding times t_{exp} when the onset of the explosion takes place and the mass accretion rate has the value of \dot{M}_{exp} . The post-bounce evolution of a collapsing star proceeds from high to low mass accretion rate (Fig. 1), i.e., from right to left on the horizontal axis of the left panel of Fig. 2. When \dot{M} reaches the critical value for the given L_{ν_e} , the model develops an explosion. The right panel of Fig. 2 visualizes the functional relations between the neutrino luminosities L_{ν_e} and the explosion times t_{exp} for both progenitors and for the simulations with different dimensions.

At first glance Fig. 2 reproduces basic trends that are visible in Figs. 17 of Murphy & Burrows (2008) and in Fig. 1 of Nordhaus et al. (2010). For example, the critical luminosity increases for higher mass accretion rate and the values for spherically symmetric models are clearly higher than those for 2D simulations. However, a closer inspection reveals interesting differences compared to the previous works.

- In general the slopes of our critical $L_{\nu_e}(\dot{M})$ -relations appear to be considerably steeper and in the case of the $15 M_{\odot}$ star they exhibit a very steep rise above $\dot{M} \approx 0.31 M_{\odot} \text{ s}^{-1}$. This means that explosions for higher mass accretion rates are much harder to obtain and therefore the tested driving luminosities in our simulations do not lead to explosions earlier than about 200 ms after bounce, independent of whether the modeling is performed in 1D, 2D or 3D. In contrast, the critical curves given by Nordhaus et al. (2010) show a moderately steep increase over the whole range of plotted mass accretion rates between about $0.1 M_{\odot} \text{ s}^{-1}$ and more than $0.5 M_{\odot} \text{ s}^{-1}$.
- Nonradial flows in the 2D case, by which the residence time of accreted matter in the gain layer could be extended or more matter could be kept in the gain region, reduce the critical luminosities by at most $\sim 15\%$ of the 1D-values for the $15 M_{\odot}$ star and $\lesssim 25\%$ for the $11.2 M_{\odot}$ model, which is a somewhat smaller difference than found by Murphy & Burrows (2008) and Nordhaus et al. (2010).
- Most important, however, is the fact that we cannot confirm the observation by Nordhaus et al. (2010) that 3D provides considerably more favorable conditions for an explosion than 2D. Our critical curves for the 2D and 3D cases nearly lie on top of each other. There are minor improvements of the explosion conditions in 3D visible in both panels of Fig. 2 and the numbers of Table 1, e.g., a 10% reduction of the smallest value of L_{ν} for which an explosion can be obtained for the $11.2 M_{\odot}$ star, a ~ 260 ms earlier explosion for the lowest luminosity driving the $15 M_{\odot}$ explosion ($2.2 \cdot 10^{52} \text{ erg s}^{-1}$),

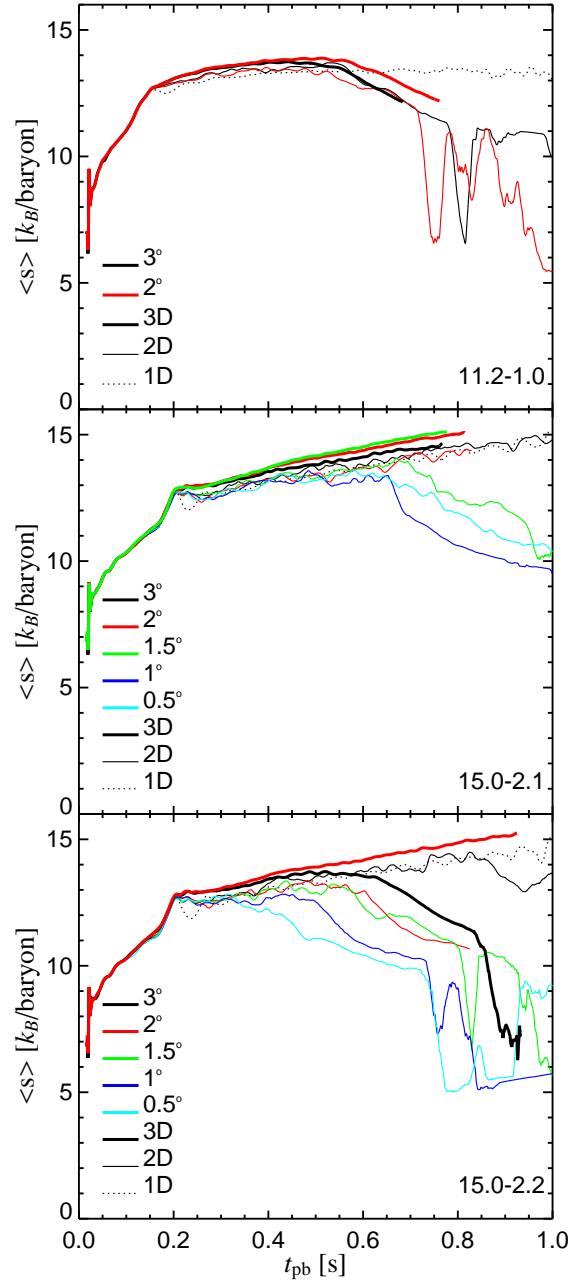


FIG. 4.— Time evolution of the mass-weighted average entropy in the gain region for one-dimensional (thin dotted lines), two-dimensional (thin solid lines), and three-dimensional (thick lines) simulations with different angular resolutions (corresponding to different colors). The top panel displays the $11.2 M_{\odot}$ results for an electron-neutrino luminosity of $L_{\nu_e} = 1.0 \cdot 10^{52} \text{ erg s}^{-1}$, the middle panel shows the $15 M_{\odot}$ runs for an electron-neutrino luminosity of $L_{\nu_e} = 2.1 \cdot 10^{52} \text{ erg s}^{-1}$, and the bottom panel the $15 M_{\odot}$ models for $L_{\nu_e} = 2.2 \cdot 10^{52} \text{ erg s}^{-1}$. The strong decrease of the average entropy that terminates a phase of continuous, slow increase signals the onset of the explosion when a growing mass of cooler (low-entropy) gas is added into the gain layer after being swept up by the expanding and accelerating shock wave.

and a tendency of slightly faster 3D explosions for all tested luminosities (see Fig. 3 and Table 1). All of these more optimistic 3D features, however, will disappear for simulations with higher resolution as we will see in Sect. 5.

Before we discuss the origin of the differences between our results and those of Murphy & Burrows (2008) and Nordhaus et al. (2010) we would like to remark that the kinks

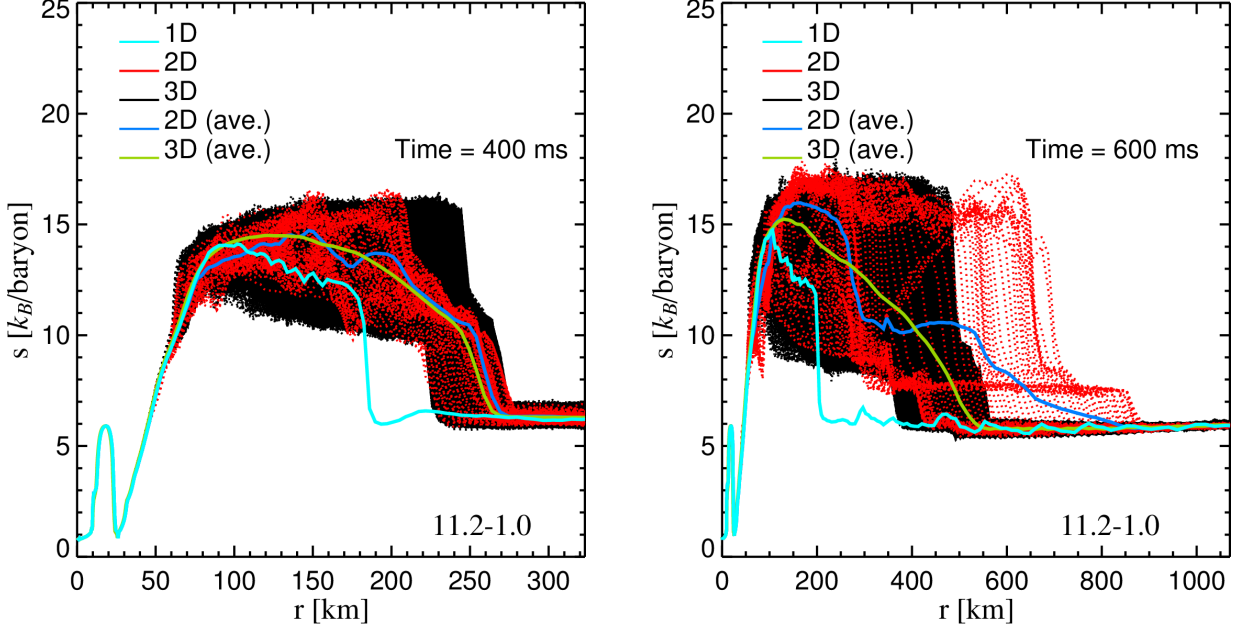


FIG. 5.— Scatter-plots of the entropy structure as function of radius for simulations of the $11.2 M_{\odot}$ progenitor with an electron-neutrino luminosity of $L_{\nu_e} = 1.0 \cdot 10^{52} \text{ erg s}^{-1}$ at 400 ms (left) and 600 ms (right) after core bounce. The red dots correspond to the 2D results, black ones to 3D, the light blue line is the entropy profile of the 1D simulation, and the dark-blue and green curves are mass-weighted angular averages of the 2D and 3D models, respectively. Both multi-dimensional simulations were performed with an angular resolution of two degrees and both yield explosions (at ~ 530 ms p.b. in 2D and ~ 570 ms p.b. in 3D; see Table 2). Note that different from Fig. 4, unshocked material at a given radius is included when computing angular averages. The dispersion of entropy values in the unshocked flow of 2D and 3D simulations is a consequence of the imposed density-seed perturbations (cf. Sect. 2), which grow in the supersonic infall regime (see Buras et al. 2006b).

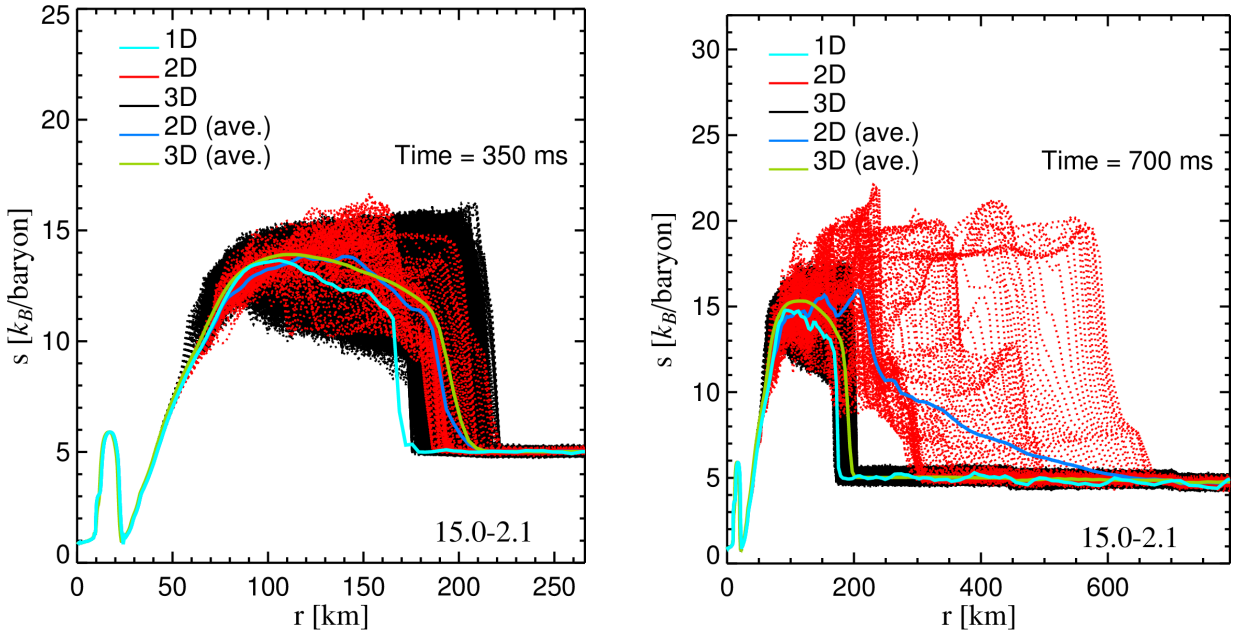


FIG. 6.— Scatter-plots of the entropy structure as function of radius for simulations of the $15 M_{\odot}$ progenitor with an electron-neutrino luminosity of $L_{\nu_e} = 2.1 \cdot 10^{52} \text{ erg s}^{-1}$ at 350 ms (left) and 700 ms (right) after core bounce. The red dots correspond to the 2D results, black ones to 3D, the light blue line is the entropy profile of the 1D simulation, and the dark-blue and green curves are mass-weighted angular averages of the 2D and 3D models, respectively. Both multi-dimensional simulations were performed with an angular resolution of 1.5 degrees. While the 2D model develops an explosion setting in ~ 720 ms after bounce, the 3D model does not produce an explosion (Table 2). Note that different from Fig. 4, unshocked material at a given radius is included when computing angular averages. The dispersion of entropy values in the unshocked flow of 2D and 3D simulations is a consequence of the imposed density-seed perturbations (cf. Sect. 2), which grow in the supersonic infall regime (see Buras et al. 2006b).

and even nonmonotonic parts of the curves shown in Fig. 2 in particular for the multi-dimensional cases are connected to our definition of the explosion time as being the moment when the mean shock radius exceeds 400 km. Especially in cases where the shock deformation is large (which is an issue mainly in some of the 2D simulations) this definition is associated with significant uncertainty in the determination of the exact explosion time t_{exp} and therefore also of the corresponding mass accretion rate \dot{M}_{exp} .

In addition to the results for our standard resolution, Fig. 2 presents 1D models with higher radial resolution (600 and 800 radial zones). The critical curves with better zoning exhibit the same overall slopes as those of the standard runs, but there is a slight shift towards higher values of the critical luminosity (or, equivalently, a small shift to lower \dot{M}_{exp} and later t_{exp}). This is caused by somewhat larger neutrino energy losses from the cooling layer with better radial resolution, an effect which makes explosions more difficult. We stress that this resolution-dependent cooling effect is a consequence of the simplified neutrino-loss treatment. The employed cooling rate is not able to reproduce real transport behavior and leads to the development of a pronounced gaussian-like density peak (with density excess of a few compared to its surroundings) in the neutrino-cooling layer. This local density maximum has a strong influence on the integrated energy loss by neutrino emission. With better zoning the peak becomes better resolved and even grows in size. Convergence of 1D results seems to be achieved for ≥ 600 radial zones, but in 2D and 3D the artificial density peak prevents numerical convergence for all employed radial zonings (cf. Sect. 5). Figure 2 also displays some data points for multi-dimensional models with better angular resolution (all of them, however, computed with 400 radial mesh points). These will be discussed in Sect. 5.

A more detailed analysis, which we will report on below and in App. A, reveals that the exact values of the critical luminosities as well as the detailed slope of the critical curves seem to depend strongly on the employed description of neutrino effects, whose implementation is subject to a significant degree of arbitrariness if detailed neutrino transport is not included in the modeling (cf. the discussion in Sect. 2). The fact that Murphy & Burrows (2008) found fairly good overall agreement between their critical relations $L_{\nu}(\dot{M})$ and those obtained by Burrows & Goshy (1993) is likely to be linked to a basically similar treatment of the neutrino effects.

Before ~ 0.2 s after bounce the mass accretion rate in the case of the $15 M_{\odot}$ progenitor changes much more rapidly than during the subsequent evolution (Fig. 1). For the corresponding \dot{M} values in excess of $\sim 0.31 M_{\odot} \text{ s}^{-1}$, the accretion shock is therefore not as close to steady-state conditions as later on. We see a steep rise of our critical curves at $\dot{M} \gtrsim 0.31 M_{\odot} \text{ s}^{-1}$ ($t_{\text{exp}} \lesssim 0.25$ s), which is a very prominent difference compared to the results of Burrows & Goshy (1993), who assumed steady-state accretion, but in particular also compared to the hydrodynamic results of Murphy & Burrows (2008), and Nordhaus et al. (2010) even in the 1D case. In order to explore possible reasons for this difference, we performed 1D simulations in which the neutrino treatment is copied from Nordhaus et al. (2010) as closely as possible (i.e., the reduction factor of 2.7 in the exponent of $e^{-\tau_{\text{eff}}}$ is not applied and deleptonization is taken into account by using a $Y_e(\rho)$ relation, but not the corresponding entropy changes proposed by Liebendörfer 2005; for more details on these results, see

App. A). These runs reveal that the steep rise of our $L_{\nu}(\dot{M})$ -curves is caused by a strong increase of the neutrino-cooling rate with higher values of \dot{M} , in particular when we apply our neutrino treatment. The corresponding energy losses inhibit explosions for low values of the driving luminosity. The stronger cooling is linked mainly to our reduction of the effective optical depth τ_{eff} , which we had to apply in order to reconcile the mass accretion rates and explosion times with the lowest driving luminosities for which Murphy & Burrows (2008) had obtained explosions for the 11.2 and $15 M_{\odot}$ stars (cf. Sect. 2). For example, in the case of the $15 M_{\odot}$ progenitor a driving luminosity of $L_{\nu_e} = 3.1 \cdot 10^{52} \text{ erg s}^{-1}$ triggers an explosion at $t_{\text{exp}} \approx 250$ ms p.b. and $\dot{M}_{\text{exp}} \approx 0.32 M_{\odot} \text{ s}^{-1}$ (Table 1 and Fig. 2), whereas with an implementation of neutrino effects closer to that of Nordhaus et al. (2010) the explosion sets in at $t_{\text{exp}} \approx 120$ ms p.b. and $\dot{M}_{\text{exp}} \approx 0.8 M_{\odot} \text{ s}^{-1}$ (see Fig. 19 in App. A). Shortly before this moment (at 75 ms after bounce) the total energy loss by neutrino cooling is about 10 times lower with the scheme of Nordhaus et al. (2010) than with our neutrino implementation. The latter yields an integrated energy-loss rate of $\sim 9 \cdot 10^{52} \text{ erg s}^{-1}$ and significant cooling even at densities between 10^{12} and $10^{13} \text{ g cm}^{-3}$, where the Nordhaus et al. (2010) treatment shows essentially no cooling. Neither the magnitude of the total neutrino-energy loss rate nor the region of energy extraction with our modeling approach are implausible and in disagreement with detailed transport simulations during a stage when the mass accretion rate still exceeds $1 M_{\odot} \text{ s}^{-1}$ (cf., e.g., Fig. 20 in Buras et al. 2006a). In contrast, the Nordhaus et al. (2010) treatment appears to massively underestimate the neutrino energy extraction from the accretion flow during this time.

These findings demonstrate that the results of the critical $L_{\nu}(\dot{M})$ -relation in 1D can be quantitatively as well as qualitatively different with different approximations of neutrino heating and in particular of neutrino cooling. Moreover, this gives reason for concern that the differences of the critical explosion conditions for 2D and 3D simulations seen by Nordhaus et al. (2010) might have been connected to their treatment of the neutrino physics, in particular also because the decrease of the critical luminosity from 2D to 3D they found was only 15–25%, which is a relatively modest change (much smaller than the 1D-2D difference) and thus could easily be overruled by other effects. Our results for 2D and 3D simulations with a different implementation of neutrino sources confirm this concern.

In the Nordhaus et al. (2010) paper the average entropy of the matter in the gain region, $\langle s(t) \rangle$, was considered to be a suitable diagnostic quantity that reflects the crucial differences of 1D, 2D, and 3D simulations concerning their relevance for the supernova dynamics. While in the spherically symmetric case accreted matter moves through the gain region on the shortest, radial paths, nonradial motions can increase the time that shock-accreted plasma can stay in the gain layer and absorb energy from neutrinos. This can raise the mean entropy, internal energy, and pressure in the postshock region and thus support the revival of the stalled supernova shock. This seems to happen in the simulations by Nordhaus et al. (2010), who found that turbulent mass motions in 3D can even improve the conditions for the neutrino-heating mechanism compared to the 2D case. A crude interpretation of this difference can be given by means of random-walk arguments, considering the mass motions in convective and turbulent structures as diffusive process in the gain layer (Murphy & Burrows 2008). The

question, however, is whether this effect is a robust 2D-3D difference and whether it is the crucial key to successful explosions by the neutrino-heating mechanism.

Our results at least raise doubts. Figure 4 displays the time evolution of the mean entropy in the gain layer for 11.2 and a 15 M_{\odot} models computed with driving luminosities near the minimum value for which we obtained explosions. While the 11.2 M_{\odot} model explodes with a luminosity of $1.0 \cdot 10^{52}$ erg s $^{-1}$ for all tested resolutions in more than one dimension despite minimal differences between the values of $\langle s(t) \rangle$ compared to the 1D counterpart, the 15 M_{\odot} progenitor develops an explosion for the chosen luminosity of $2.1 \cdot 10^{52}$ erg s $^{-1}$ only in the case of higher-resolution 2D runs (this will be further discussed in Sect. 5). These successful cases, however, do not stick out by especially high values of $\langle s(t) \rangle$. On the contrary, they even have lower mean entropies than the unsuccessful 3D models! It is obvious that Fig. 4 does not exhibit the clear 1D-2D-3D hierarchy visible in Fig. 5 of the Nordhaus et al. (2010) paper, which was found there to closely correlate with the explosion behavior of their models. Instead, the differences between simulations in the different dimensions are fairly small, and even two-dimensional flows, which unquestionably allow for explosions also when none happen in 1D, do not appear more promising than the 1D case in terms of the average entropy of the matter in the gain layer². Similarly, 3D models possess slightly (insignificantly?) higher values of $\langle s(t) \rangle$ but do not show a clear tendency of easier explosions, in particular not the better resolved simulations (see Sect. 5).

The radial entropy structures of 1D, 2D, and 3D runs for both progenitors, shown in Figs. 5 and 6 once before an explosion begins and another time around the onset of an explosion in at least one of the runs, demonstrate that low-entropy accretion downdrafts and high-entropy rising plumes of neutrino-heated plasma lead to large local variations of the entropy per baryon of the matter in the gain layer (scatter regions in the plots). However, the mass-weighted angular averages of the entropies reveal much smaller differences between the 1D and 2D cases than visible in Fig. 4 of the Nordhaus et al. (2010) paper and in Fig. 13 of Murphy & Burrows (2008), and exhibit no obvious signs of more advantageous explosion conditions in the 3D cases compared to 2D. The noticeable differences in the radial profiles seem to be insufficient to cause major differences in the mean entropies computed by additional radial averaging (see Fig. 4).

How can this discrepancy compared to Nordhaus et al. (2010) and Murphy & Burrows (2008) be explained, and how can one understand the fact that 2D effects play a supportive role for neutrino-driven explosions? We will return to these questions in Sect. 6, but before that we shall present our results of multi-dimensional simulations with varied resolution in the following section.

5. MODELS WITH HIGHER RESOLUTION

In order to test whether our results for the multi-dimensional models depend on the agreeably moderate 3° angular resolution used in the standard runs, we performed a large set of simulations with finer grid spacing especially in the angular directions, but also in radial direction. For this

² We stress that our basic findings are independent of the exact way how the gain radius of the multi-dimensional models is determined, i.e., whether the evaluation is performed with an angularly averaged gain radius or a direction-dependent gain radius. The outer boundary of the integration volume is defined by the shock position, which usually forms a non-spherical surface in the multi-dimensional case.

TABLE 2
MULTIDIMENSIONAL MODELS WITH DIFFERENT RESOLUTION.

Mass ^a (M_{\odot})	Dim ^b	L_{ν_e} ^c (10^{52} erg/s)	Ang. ^d Res.	N_r ^e	t_{exp} ^f (ms)	\dot{M}_{exp} ^g	t_{sim} ^h (ms)
11.2	2D	0.8	3°	400	–	–	1017
11.2	2D	0.8	2°	400	–	–	979
11.2	3D	0.8	3°	400	–	–	915
11.2	3D	0.8	2°	400	–	–	758
11.2	2D	0.9	3°	400	–	–	1006
11.2	2D	0.9	2°	400	–	–	985
11.2	3D	0.9	3°	400	731	0.085	954
11.2	3D	0.9	2°	400	–	–	819
11.2	2D	1.0	3°	400	563	0.082	1053
11.2	2D	1.0	2°	400	527	0.086	1053
11.2	3D	1.0	3°	400	537	0.086	684
11.2	3D	1.0	2°	400	572	0.082	761
15	2D	2.0	3°	400	–	–	1016
15	2D	2.0	2°	400	–	–	829
15	2D	2.0	1.5°	400	–	–	1016
15	2D	2.0	1°	400	–	–	1016
15	3D	2.0	3°	400	–	–	723
15	3D	2.0	2°	400	–	–	524
15	2D	2.1	3°	400	–	–	1016
15	2D	2.1	2°	400	–	–	829
15	2D	2.1	1.5°	400	719	0.210	1016
15	2D	2.1	1°	400	575	0.232	1016
15	2D	2.1	0.5°	400	657	0.220	1016
15	3D	2.1	3°	400	–	–	767
15	3D	2.1	2°	400	–	–	815
15	3D	2.1	1.5°	400	–	–	777
15	2D	2.2	3°	400	876	0.197	1016
15	2D	2.2	2°	400	557	0.238	825
15	2D	2.2	1.5°	400	556	0.239	1016
15	2D	2.2	1°	400	424	0.262	1016
15	2D	2.2	0.5°	400	365	0.288	1016
15	3D	2.2	3°	400	612	0.226	932
15	3D	2.2	2°	400	–	–	925
15	2D	2.1	3°	600	–	–	1016
15	2D	2.1	3°	800	–	–	1016
15	2D	2.1	2°	600	–	–	1016
15	2D	2.1	2°	800	–	–	1016
15	2D	2.1	1.5°	600	–	–	1016
15	2D	2.1	1.5°	800	–	–	1016
15	2D	2.1	1°	600	780	0.203	1016
15	2D	2.1	1°	800	–	–	1016
15	2D	2.1	0.5°	600	749	0.211	1016
15	2D	2.1	0.5°	800	886	0.198	1016
15	3D	2.1	3°	600	–	–	946
15	3D	2.1	3°	800	–	–	958
15	2D	2.2	3°	600	–	–	1016
15	2D	2.2	3°	800	–	–	1016
15	2D	2.2	2°	600	683	0.218	1016
15	2D	2.2	2°	800	–	–	1016
15	2D	2.2	1.5°	600	713	0.215	1016
15	2D	2.2	1.5°	800	863	0.196	1016
15	2D	2.2	1°	600	761	0.214	1016
15	2D	2.2	1°	800	961	0.194	1016
15	2D	2.2	0.5°	600	588	0.232	1016
15	2D	2.2	0.5°	800	643	0.224	1016
15	3D	2.2	3°	600	803	0.202	975
15	3D	2.2	3°	800	857	0.195	977
15	3D	2.2	2°	600	–	–	988
15	3D	2.2	1.5°	800	–	–	898

^a Progenitor model.

^b Dimensionality.

^c Electron-neutrino luminosity.

^d Angular Resolution.

^e Number of radial zones.

^f Time of onset of explosion.

^g Mass accretion rate at onset of explosion.

^h Simulation time.

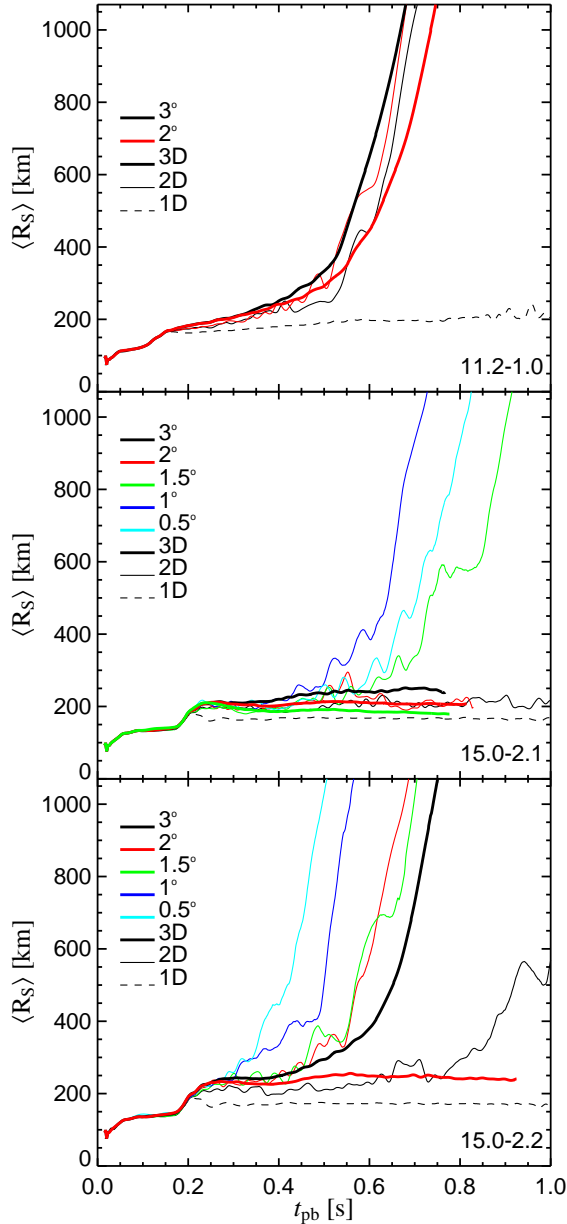


FIG. 7.— Evolution of the average shock radius as a function of time (in seconds after bounce) for one-dimensional (dashed lines), two-dimensional (thin solid lines) and three-dimensional (thick solid lines) simulations employing different angular resolutions (color coding). The top panel displays the $11.2 M_{\odot}$ model for an electron-neutrino luminosity of $L_{\nu_e} = 1.0 \cdot 10^{52} \text{ erg s}^{-1}$, the middle panel shows the $15 M_{\odot}$ star for an electron-neutrino luminosity of $L_{\nu_e} = 2.1 \cdot 10^{52} \text{ erg s}^{-1}$, and the bottom panel the $15 M_{\odot}$ results for $L_{\nu_e} = 2.2 \cdot 10^{52} \text{ erg s}^{-1}$.

purpose we concentrated on cases around the minimum values of the driving luminosity that triggered explosions of both progenitors in our standard runs. The results are listed in Table 2. They indicate a very interesting trend: 2D models with finer angular zoning tend to explode more readily, whereas better angular resolution in 3D simulations turns out to have the opposite effect.

In the case of the $11.2 M_{\odot}$ progenitor, for example, the 3D explosion found to set in at about 730 ms p.b. with an angular zone size of 3° for $L_{\nu_e} = 0.9 \cdot 10^{52} \text{ erg s}^{-1}$ cannot be reproduced with an angle binning of 2° . Moreover, a luminosity of $L_{\nu_e} = 1.0 \cdot 10^{52} \text{ erg s}^{-1}$ leads to an explosion of the 3D model

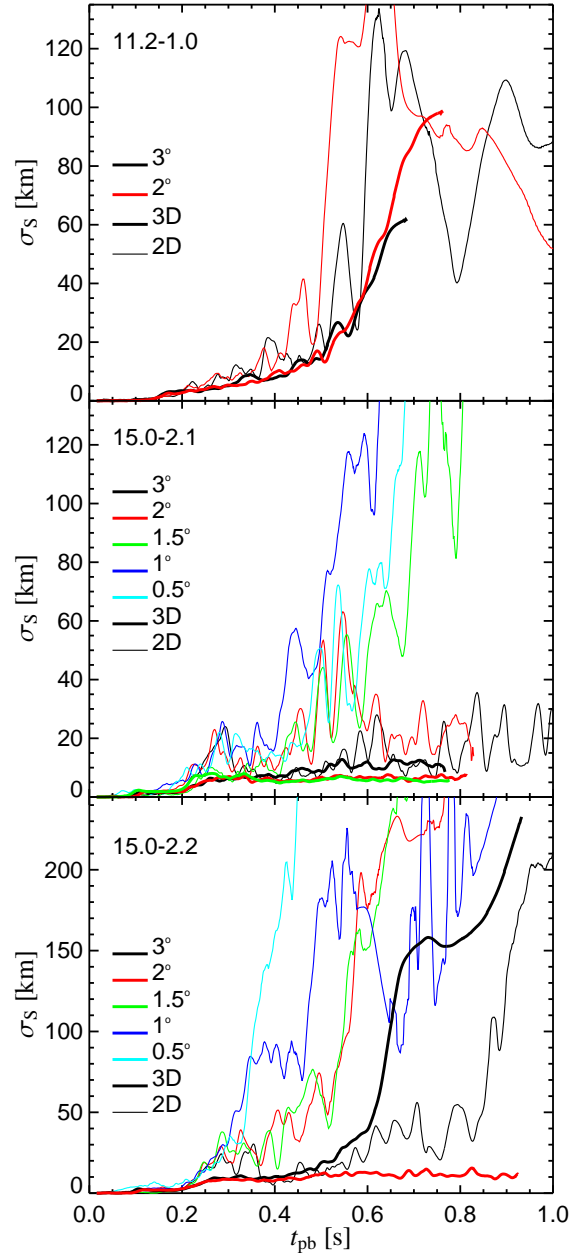


FIG. 8.— Evolution of the standard deviation for the shock asphericity as a function of post-bounce time for two-dimensional (thin solid lines) and three-dimensional (thick solid lines) simulations employing different angular resolutions (color coding). As in Fig. 7 the top panel displays the exploding $11.2 M_{\odot}$ models for an electron-neutrino luminosity of $L_{\nu_e} = 1.0 \cdot 10^{52} \text{ erg s}^{-1}$. The middle panel contains the results for the $15 M_{\odot}$ star with an electron-neutrino luminosity of $L_{\nu_e} = 2.1 \cdot 10^{52} \text{ erg s}^{-1}$, where 2D runs with higher resolution lead to explosions while 3D runs do not. The bottom panel shows the $15 M_{\odot}$ case for $L_{\nu_e} = 2.2 \cdot 10^{52} \text{ erg s}^{-1}$. It is remarkable that the 3D run with 2° angular resolution does not explode whereas the one with angle bins of 3° explodes earlier than its 2D counterpart and develops a very large shock deformation at the time the explosion sets in.

at ~ 540 ms after bounce with a 3° -grid, but ~ 35 ms later when 2° are used. The corresponding 2D models show the inverse trend as visible in the top panel of Fig. 7.

Note that the average shock radii plotted in Fig. 7 as well as Fig. 3 exhibit alternating periods of increase and decrease in particular in 2D simulations. Such features are a consequence of the strong sloshing motions of the accretion shock and of the associated time-dependent, large global shock de-

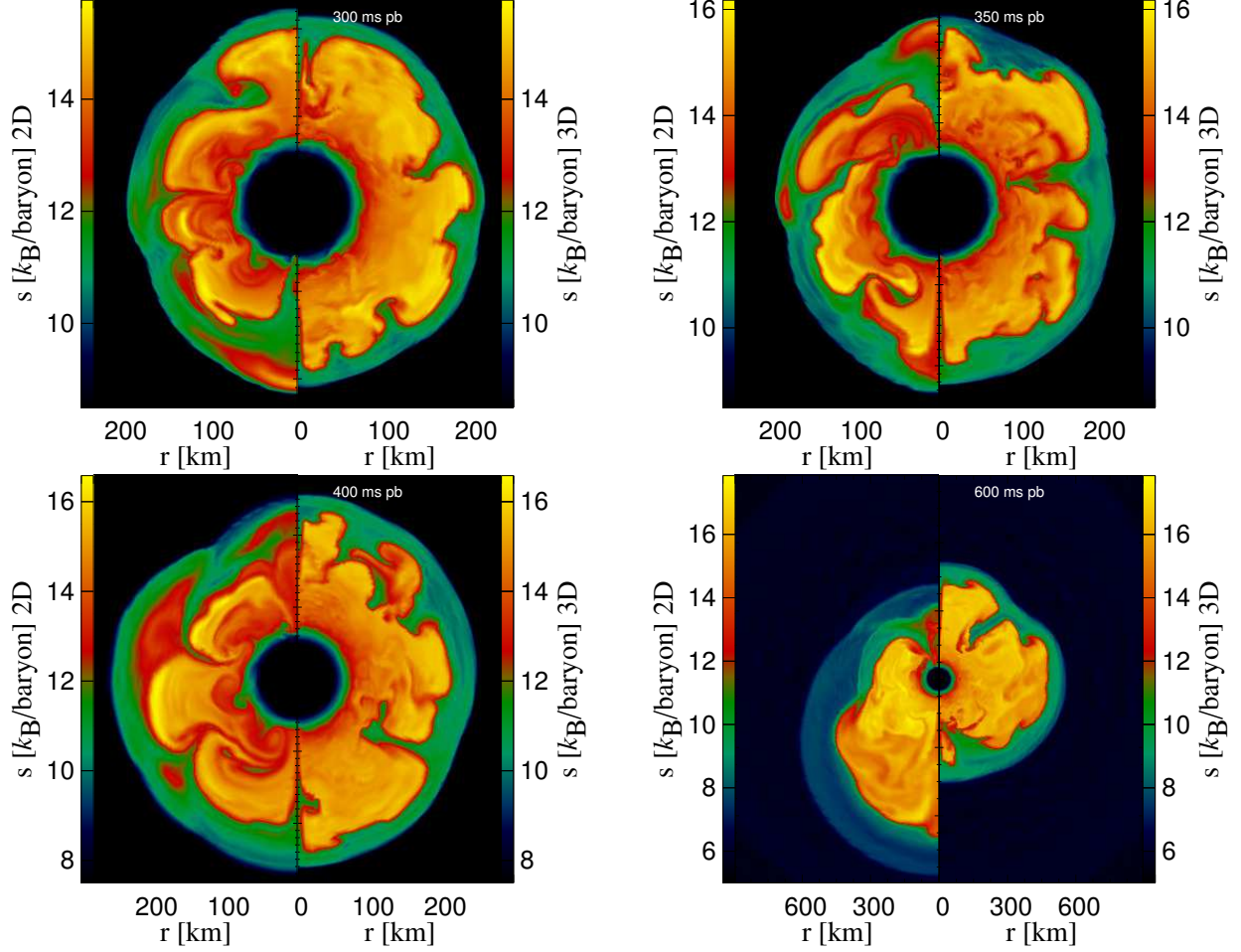


FIG. 9.— Snapshots of the evolution of the $11.2 M_{\odot}$ model with an electron-neutrino luminosity of $L_{\nu_e} = 1.0 \cdot 10^{52} \text{ erg s}^{-1}$ and 2° angular resolution at post-bounce times of $t_{\text{pb}} = 300, 350, 400,$ and 600 ms (from top left to bottom right). The color coding represents the entropy per nucleon of the stellar plasma. The left half of each panel displays the entropy distribution for a 2D (axisymmetric) simulation, the right half shows the structure in a meridional cut of the corresponding 3D simulation. Both models explode after roughly 550 ms after bounce (see Fig. 7, top panel, and Table 2). Note that the structures of low-entropy downdrafts and high-entropy plumes in the neutrino-heating region are rather similar for both cases, despite considerably larger SASI sloshing motions of the shock and postshock layer in 2D. When the explosion has set in, the 2D model exhibits an apparent prolate deformation whose development is supported by the symmetry axis defining a preferred direction of the 2D system. While the 3D explosion does not appear to be as strongly distorted (in particular the shock surface looks more spherical), the postshock flow in this case also develops a pronounced hemispheric (dipolar) asymmetry, which can be more clearly seen in the upper and lower right panels of Fig. 10.

formations, which are typical of violent activity by the SASI. In 3D the corresponding wiggles and local maxima of the average shock trajectory are much less pronounced. A measure of the degree of shock asphericity, irrespective of the relative weights of different spherical harmonics components, is the standard deviation of the shock radius defined by $\sigma_S \equiv \sqrt{\frac{1}{4\pi} \oint d\Omega [R_S(\vec{\Omega}) - \langle R_S \rangle]^2}$. The standard deviations corresponding to the average shock radii of Fig. 7 are plotted in Fig. 8, which confirms the mentioned difference between 2D and 3D runs.

In spite of this 2D-3D difference of the shock asphericity, an inspection of cross-sectional snapshots of our best resolved simulations of the $11.2 M_{\odot}$ progenitor with an electron-neutrino luminosity of $L_{\nu_e} = 1.0 \cdot 10^{52} \text{ erg s}^{-1}$ reveals that the sizes of the convective plumes and the structure of the neutrino-heated postshock layer are fairly similar in the 2D and 3D cases before explosion (which in both models develops shortly after 500 ms): In Fig. 9 it is difficult to judge by eye inspection whether the displayed simulation was conducted in 2D (left half-panels) or 3D (right half-panels). Even

after the explosions have taken off the global deformation of the shock in both cases is not fundamentally different in the sense that low-order spherical harmonics modes (dipolar and quadrupolar components) determine the global asymmetry of the shock surface and in particular of the distribution of downdrafts and expanding bubbles in the gain region (see Fig. 9, lower right panel, and Fig. 10). At a closer inspection one can notice some secondary differences in the morphology of the convective and downflow features. Despite the same angular resolution the images of Figs. 9 and 10 reveal more small structures in the 3D case compared to the 2D data, which appear more coherent, smoother, and less fragmented into finer substructures and filaments. We will refer to this observation in Sect. 6.

Our $15 M_{\odot}$ runs with varied resolution confirm the trends seen for the $11.2 M_{\odot}$ progenitor. For a neutrino luminosity of $L_{\nu_e} = 2.1 \cdot 10^{52} \text{ erg s}^{-1}$, for which neither 2D nor 3D simulations with standard resolution produce an explosion, we find that 2D models with angular binning of 1.5° or better do explode, whereas explosions in 3D cannot be obtained with angular zones in the range from 1.5° to 3° (Fig. 7, middle

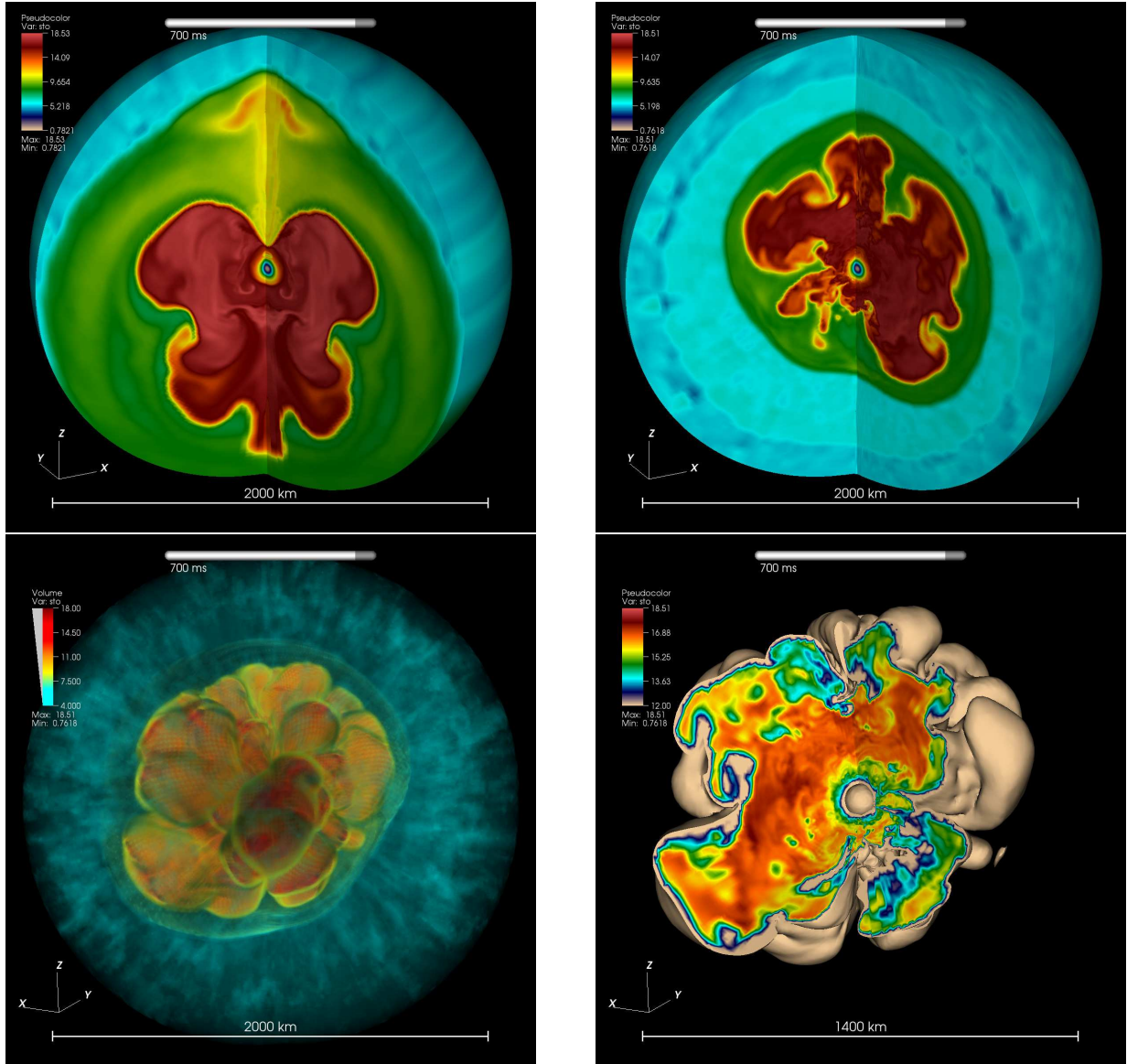


FIG. 10.— *Upper row*: Quasi-three-dimensional visualization of the $11.2 M_{\odot}$ simulations in 2D (upper left panel) and 3D (upper right panel) with an electron-neutrino luminosity of $L_{\nu_e} = 1.0 \cdot 10^{52} \text{ erg s}^{-1}$ and an angular resolution of 2° , comparing the structure at 700 ms p.b., roughly 150 ms after the onset of the explosions. Since the explosion started slightly earlier in the 2D model (see the upper panel of Fig. 7 and Table 2) the shock is more extended in the left image. While in this case the shock possesses a much stronger dipolar deformation component than in 3D (cf. Fig. 9, lower right panel), the distribution of accretion funnels and plumes of neutrino-heated matter exhibits a hemispheric asymmetry in both cases. Because of the axisymmetry of the 2D geometry this concerns the hemispheres above and below the x - y -plane in the upper left plot, whereas the virtual equator lies in the plane connecting the upper left and lower right corners of the top right image and the lower left and upper right corners of the bottom right picture. Note that the jet-like axis feature in the upper left figure is a consequence of the symmetry constraints of the 2D setup, which redirect flows moving towards the polar grid axis. Such artifacts do not occur in the 3D simulation despite the use of a polar coordinate grid there, too. *Lower row*: Ray-tracing and volume-rendering images of the three-dimensional explosion of the $11.2 M_{\odot}$ progenitor for the same simulation and time displayed in the upper right image. The left lower panel visualizes the outer boundaries of the buoyant bubbles of neutrino-heated gas and the outward driven shock, which can be recognized as a nearly transparent, enveloping surface. The visualization uses the fact that both are entropy discontinuities in the flow. The infalling matter in the preshock region appears as diffuse, nebular cloud. The right lower panel displays the interior structure by the entropy per nucleon of the plasma (red, yellow, green, light blue, dark blue correspond to decreasing values) within the volume formed by the high-entropy bubbles, whose surface is cut open by removing a wide cone facing the observer. Note the clear dipolar anisotropy with stronger explosion towards the north-west direction and more accretion at the south-east side of the structure.

panel; Table 2). The 2D simulations exhibit violent SASI sloshing motions and the quasi-periodic appearance of large shock asymmetries (Fig. 8, middle panel), and the 2D model with 1.5° angular zoning explodes with a huge prolate deformation (Fig. 11). A similar behavior is seen for the $15 M_{\odot}$ runs with $L_{\nu_e} = 2.2 \cdot 10^{52} \text{ erg s}^{-1}$: While all 2D models computed with angular zone sizes between 0.5° and 3° explode, we observe an explosion for the 3D calculation with 3° but none for the case with 2° angular binning (Table 2 and Fig. 7,

bottom panel). It is highly interesting that the 3° case, where the explosion occurs more readily in 3D than in 2D, is associated with a large asphericity of the supernova shock at the time the 3D run begins to develop the successful blast (Fig. 8, bottom panel). Note again that the structures of the higher-resolved 3D model in Fig. 11 reveal finer details and fragmentation into smaller filaments than the corresponding 2D simulation, despite both having the same zone sizes in the angular directions.

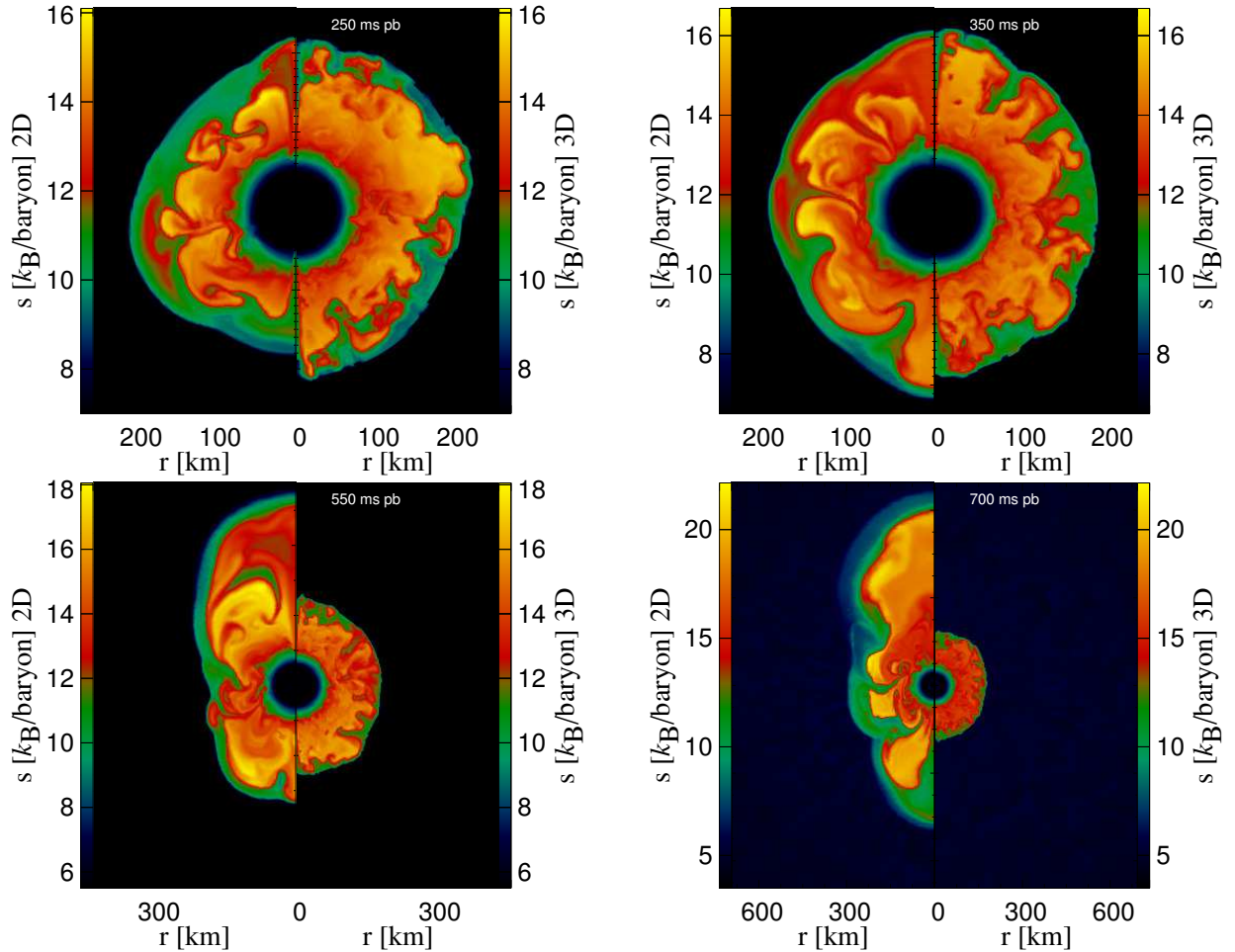


FIG. 11.— Snapshots of the post-bounce evolution of the $15 M_{\odot}$ model with an electron-neutrino luminosity of $L_{\nu_e} = 2.1 \cdot 10^{52} \text{ erg s}^{-1}$ and angular resolution of 1.5° at $t_{\text{pb}} = 250, 350, 550,$ and 700 ms. The color coding represents the entropy per nucleon of the stellar gas. The left half of each panel shows the entropy distribution for a 2D simulation, and the right half displays a meridional cut from the corresponding 3D model. While the 2D run with the given resolution leads to a highly prolate explosion, the 3D calculation does not end in a successful blast (see Fig. 7, middle panel, and Table 2). Note that the convective plumes are considerably smaller and more fine-structured in the 3D simulation.

The data listed in Table 2 contain the clear message that 2D models with better angular resolution usually develop explosions earlier in contrast to 3D runs, which explode later or not at all when the angular zoning is finer. There can be 2D exceptions to the general trend (e.g., the $15 M_{\odot}$ cases with $L_{\nu_e} = 2.1 \cdot 10^{52} \text{ erg s}^{-1}$ and 0.5° and 1° resolution for 400 radial zones; see also Fig. 7, middle panel), which are either affected by the difficulty to exactly determine the onset of the blast in cases with a highly deformed shock, or which can be stochastic outliers associated with the chaotic processes leading to the explosion. Note in this context that at late times $\dot{M}(t)$ is very flat and therefore differences in t_{exp} correspond to only small differences in \dot{M}_{exp} . For this reason the beginning of the explosion can be shifted by minor perturbations, e.g. connected to stochastic fluctuations. It is also possible that for special circumstances the symmetry axis of the 2D geometry has an influence on such a non-standard behavior because of its effect to redirect converging flows outwards or inwards and thus to have a positive feedback on the violence of the SASI activity.

Improved radial resolution for fixed angular grid turns out to have a negative influence on the possibility of an explosion also in multi-dimensional simulations. 2D runs with better radial zoning (600 or even 800 instead of 400 radial zones)

fail to develop explosions or explode significantly later than their less well resolved counterparts (see the $15 M_{\odot}$ results for $L_{\nu_e} = 2.1 \cdot 10^{52} \text{ erg s}^{-1}$ and $2.2 \cdot 10^{52} \text{ erg s}^{-1}$ in Table 2). In general, in 1D, 2D, and 3D improved radial resolution shifts the onset of the explosion to later times monotonically. The only successful 3D model in the set that is useful for the present discussion, a $15 M_{\odot}$ run with $L_{\nu_e} = 2.2 \cdot 10^{52} \text{ erg s}^{-1}$ and 3° angular resolution, supports our findings in 2D. It shows an increasingly delayed explosion for better radial resolution, although the results with 600 and 800 radial zones appear to be nearly converged. All non-exploding 3D models do not yield successes also with higher radial resolution.

The conclusion that good radial resolution is very important for reliable results, in particular when the explosion is “marginal”, would not be a surprise, because Sato et al. (2009) have pointed out the importance of the radial zoning close to the neutron star and around the supernova shock in order to accurately capture the entropy and vorticity production at the shock and to determine growth times and oscillation frequencies of the SASI. The latter is unquestionably an essential ingredient for the success of the neutrino-driven mechanism in our 2D runs and it may as well be a crucial component for the mechanism to work in 3D. As mentioned in Sect. 4, however, the sensitive influence of the radial zoning in the

discussed model set is mainly a consequence of an artificial density peak developing in the neutrino-loss region because of the use of the simplified neutrino-cooling treatment. The narrow shape of this numerical artifact in the density structure, which enhances the energy emission by neutrinos, can even cause a dependence of the results on the particular choice of the grid-cell locations. Different from the 1D runs the results of multi-dimensional simulations with more than ~ 600 radial zones do not seem to converge. Since the local density maximum lies between $10^{12} \text{ g cm}^{-3}$ and $10^{13} \text{ g cm}^{-3}$ in the core that is treated spherically symmetrically in our simulations, we interpret this phenomenon as the consequence of a subtle feedback between higher zoning and cooling strength on the one hand and multi-dimensional processes in the accretion layer on the other hand. Because of the artificial nature of the underlying density feature, however, we did not further explore this finding.

Finally, we remark that prior to our present work Scheck (2007) has already performed resolution studies with a large set of 2D simulations, in which he varied the lateral zone width between 0.5° and 4° . In addition, he conducted three 3D simulations with angular bin sizes of $2\text{--}4^\circ$. However, instead of the highly simplified heating and cooling description used by us he employed the much more sophisticated approximation for grey neutrino transport described in detail in Scheck et al. (2006). This approximation included, e.g., the feedback of accretion on the neutrino emission properties and on the corresponding energy and lepton number transport by neutrinos and antineutrinos of all flavors, as well as a more elaborate description of neutrino-matter interactions in detailed dependence on the thermodynamical state of the stellar plasma. Scheck (2007) was not interested in a systematic exploration of the critical explosion condition, but his project was focussed on investigating the possibility of hydrodynamic pulsar kicks by successful asymmetric explosions. Despite the grave differences of the neutrino treatments and numerical setups, the results obtained by Scheck (2007) are compatible with our present findings: 2D simulations with higher resolution turned out to yield explosions significantly earlier and thus also more energetically than the low-resolution runs. Within the tested range of angular resolutions Scheck (2007) did not observe any significant differences between his 3D models. This, however, may just be a consequence of the fact that the models were clearly above the threshold conditions for an explosion and did not linger along the borderline between blast and failure.

6. INTERPRETATION AND DISCUSSION

In this section we discuss the meaning of our results in comparison to previous studies and present an interpretation that could explain the main trends found in our multi-dimensional simulations with varied resolution.

6.1. Variation with dimension

In Sects. 4 and 5 we have reported that our simulations do not support the central finding by Nordhaus et al. (2010) that the tendency to explode is a monotonically increasing function of dimension. While we confirm more favorable explosion conditions in 2D than in 1D, we do not observe that in 3D considerably lower driving luminosities are needed for a success of the neutrino-driven mechanism than in 2D. Moreover, we cannot confirm the finding by Nordhaus et al. (2010) that the mass-weighted average of the entropy per nucleon in the gain region, $\langle s(t) \rangle$, is a quantity that is suitable as an indicator

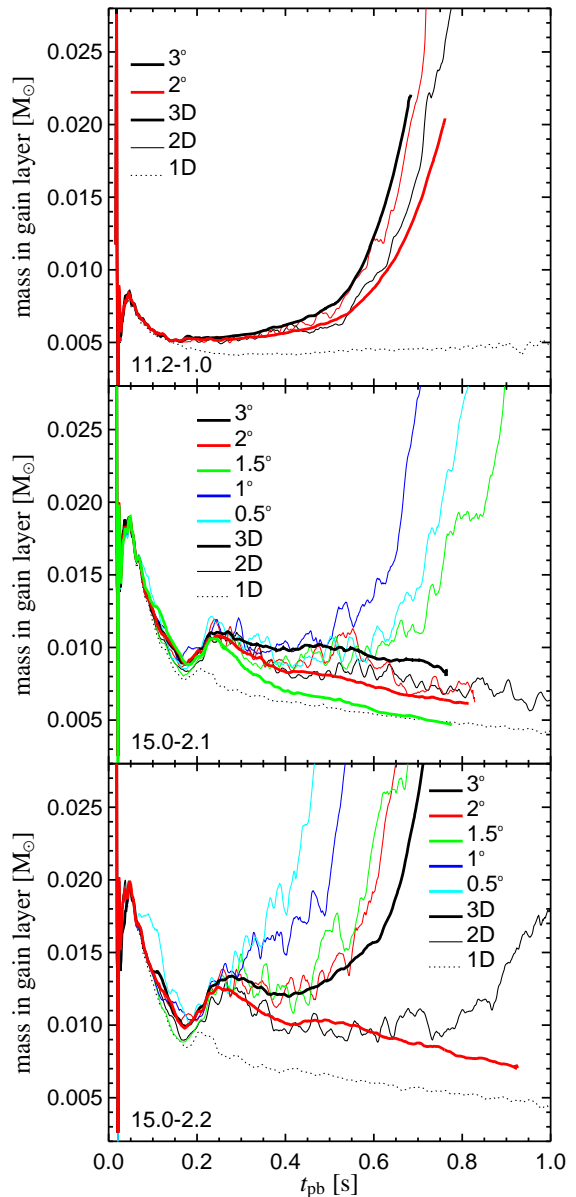


Fig. 12.— Time evolution of the mass in the gain region (in seconds after bounce) for simulations in 1D (thin dotted line), 2D (thin solid lines), and 3D (thick lines). The multi-dimensional models are displayed for all employed angular resolutions depicted by different colors. The top panel shows the results for the $11.2 M_\odot$ star with an electron-neutrino luminosity of $L_{\nu_e} = 1.0 \cdot 10^{52} \text{ erg s}^{-1}$, the middle panel the results for the $15 M_\odot$ runs with $L_{\nu_e} = 2.1 \cdot 10^{52} \text{ erg s}^{-1}$, and the bottom panel the $15 M_\odot$ models for $L_{\nu_e} = 2.2 \cdot 10^{52} \text{ erg s}^{-1}$. The different cases are the same as in Figs. 7 and 8.

of the proximity of models to an explosion and thus can serve as an explanation of differences between 1D, 2D, and 3D simulations. In particular, our 3D models turned out to have slightly higher mean entropies than corresponding 2D cases (Fig. 4) without developing better explosion conditions. This raises the question why our models, and multi-dimensional simulations in general, have produced successful explosions by the neutrino-heating mechanism when corresponding 1D models fail?

It is by no means obvious that $\langle s(t) \rangle$ should increase in the gain layer in the multi-dimensional case. While neutrino energy deposition naturally leads to a rise of the entropy of the heated gas, the averaging process over the volume of the gain

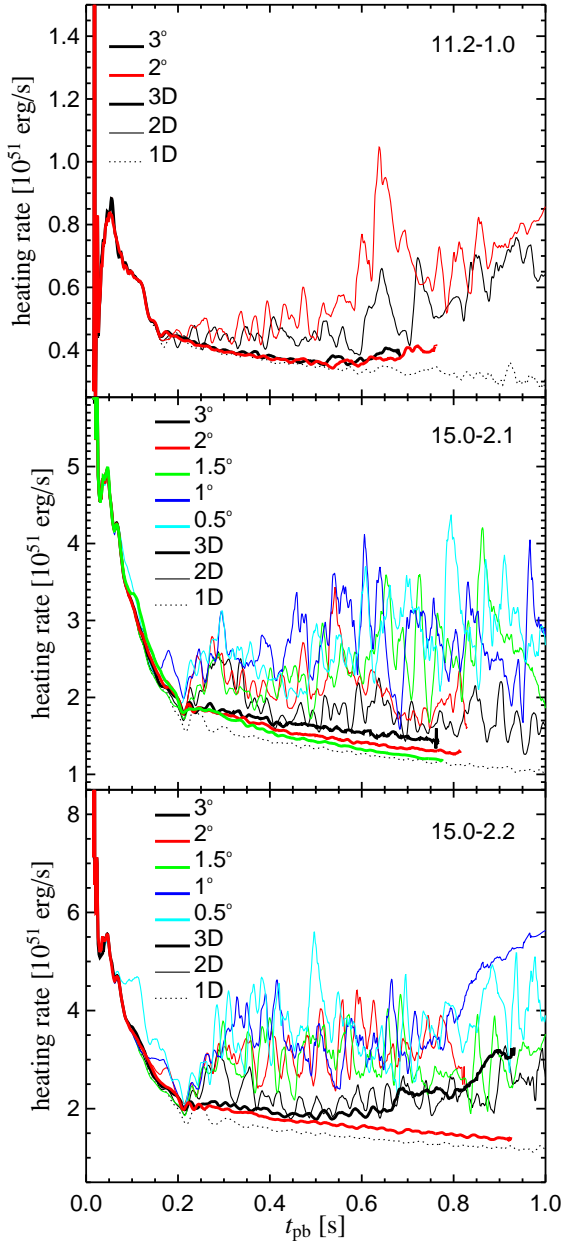


FIG. 13.— Analogous to Fig. 12, but for the time evolution of the total net rate of neutrino heating in the gain region.

layer also encompasses the downdrafts carrying cool matter from the postshock region towards the gain radius and the neutron star. These downdrafts are much denser, they are hardly heated by neutrinos because of their extremely rapid infall, and they can contain more mass than the surrounding, dilute bubbles that are inflated by the expanding, neutrino-heated plasma. It is therefore not clear that the spatial (mass-weighted) average $\langle s(t) \rangle$ grows in multi-dimensions compared to 1D runs.

Moreover, it is not even clear that convective overturn in the gain layer must lead to an average entropy of the neutrino-heated gas itself that is higher than in 1D simulations. Different from the 1D case high-entropy matter becomes buoyant and begins to float in the multi-dimensional environment. Thus the heated gas is quickly carried away from the vicinity of the gain radius, where neutrino-energy deposition is maximal, to larger radii. Such dynamics of the gas can well limit

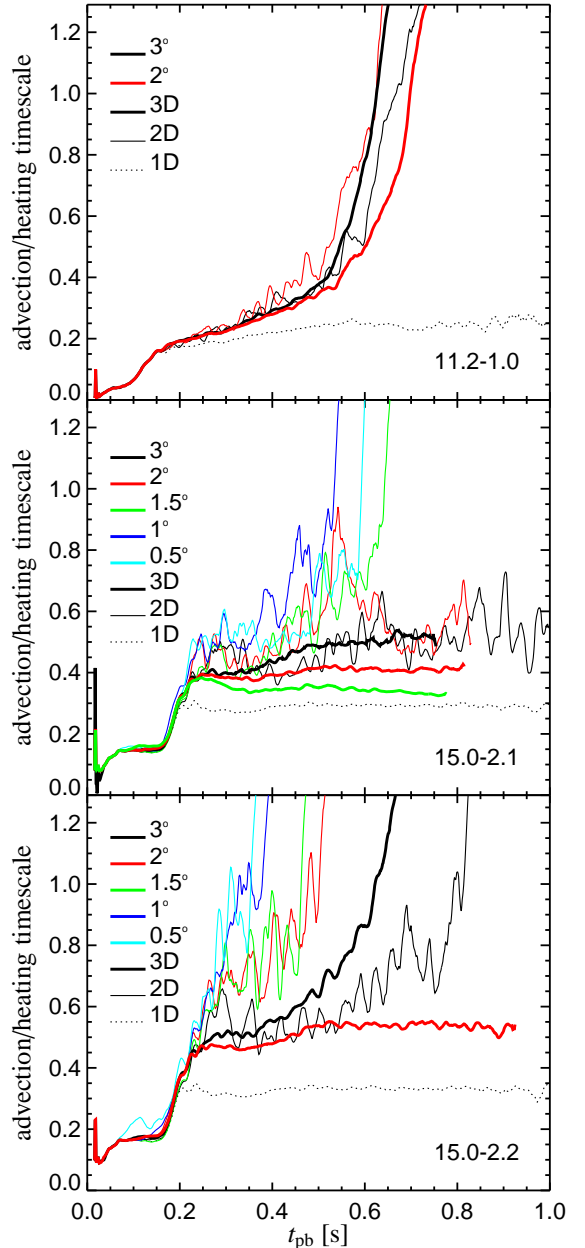


FIG. 14.— Analogous to Fig. 12, but for the time evolution of the ratio of advection timescale to heating timescale in the gain layer.

the amount of energy and entropy that is stored in individual chunks of matter. Little, if any of the gas is subject to multiple overturn cycles bringing the gas close to the gain radius more than once as suggested by the “convective engine” picture of Herant et al. (1994) but questioned by Burrows et al. (1995). Instead, the majority of the heated gas either expands to larger distances, pushing shock expansion, or, in the disadvantageous case, is swept back below the gain radius (e.g. by large-amplitude sloshing motions of the shock), where it loses its energy again by efficiently reradiating neutrinos³.

Our results imply that the dominant effect that makes the

³ The real multi-dimensional situation is even more complicated. The mentioned violent sloshing motions of the shock can cause strong shock-heating of the postshock matter as discussed in detail by Scheck et al. (2008), Blondin et al. (2003), and Blondin & Mezzacappa (2006b), thus not only massively affecting the postshock flow but also providing an additional entropy source besides neutrino-energy deposition.

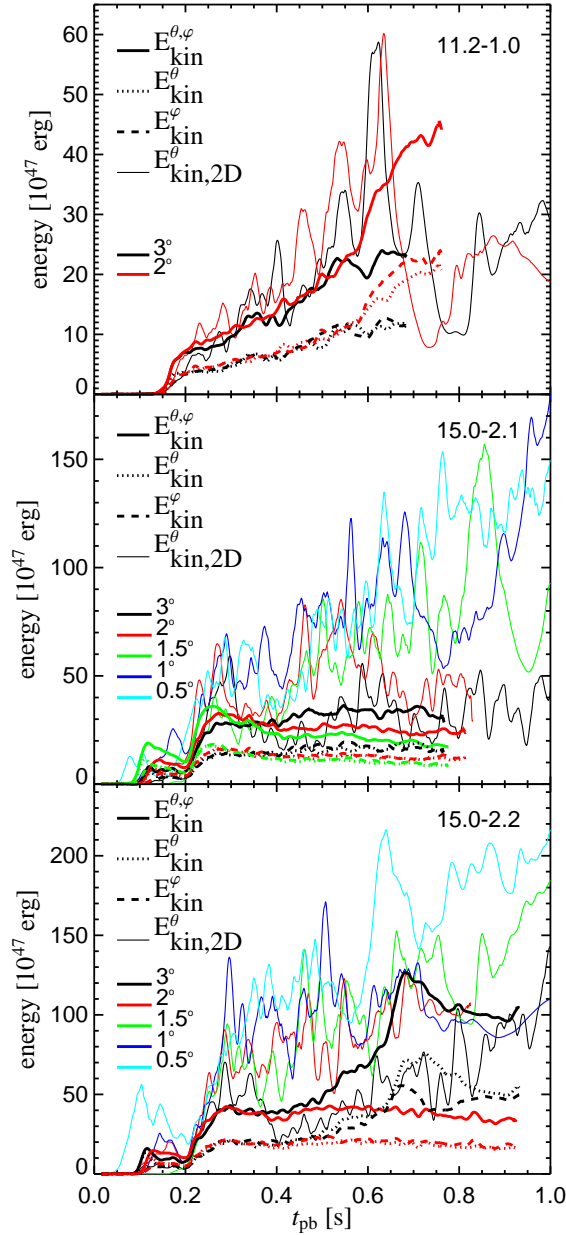


FIG. 15.— Kinetic energies of angular mass motions in the gain layer as functions of time after bounce for the $11.2 M_{\odot}$ runs with an electron-neutrino luminosity of $L_{\nu_e} = 1.0 \cdot 10^{52} \text{ erg s}^{-1}$ (top panel) and the $15 M_{\odot}$ runs with $L_{\nu_e} = 2.1 \cdot 10^{52} \text{ erg s}^{-1}$ (middle panel) and $L_{\nu_e} = 2.2 \cdot 10^{52} \text{ erg s}^{-1}$ (bottom panel). Thin solid lines correspond to the lateral kinetic energy of 2D models, while for 3D simulations (thick lines) the lateral, azimuthal, and total kinetic energies are represented by dotted, dashed, and solid line styles, respectively. Both angular directions contribute essentially equally to the total kinetic energy of nonradial motions in the 3D case. As in Figs. 7, 8, 12, and 13, different colors depict different angular resolutions. It is visible that for models closer to a success of the neutrino-driven mechanism the angular kinetic energy exhibits larger temporal variations and an overall trend of increase as the onset of the explosion is approached.

multi-dimensional case more favorable for an explosion than spherical symmetry is associated with an inflation of the shock radius and postshock layer, driven by the buoyant rise and expansion of the plumes of neutrino-heated plasma. In course of the postshock volume becoming more extended, the integrated mass M_{gain} in the heating layer increases compared to the 1D case. This can be seen in Fig. 12, which displays the mass in the gain layer as function of post-bounce time for

the 11.2 and $15 M_{\odot}$ runs with the different neutrino luminosities and resolutions already shown in Figs. 7 and 8. While the mass-averaged entropy $\langle s \rangle$ in the gain region hardly changes, the integral value of the entropy, $M_{\text{gain}} \langle s \rangle$, clearly increases with models coming closer to explosion. This dependence is particularly well visible when 2D and 3D models with different resolutions are compared with each other.

The longer dwell times of matter in the gain layer of 2D simulations observed by Murphy & Burrows (2008), which correspond to the advection times τ_{adv} evaluated by Buras et al. (2006b) and Marek & Janka (2009) (though different ways of calculation have been considered, in particular for the multi-dimensional case), are a manifestation that a growing mass accumulates in the postshock region to get energy-loaded by neutrino absorption and to finally drive the successful supernova blast. In near-steady-state conditions the mass accretion rate through the gain layer is equal to the mass infall rate \dot{M} ahead of the shock, where it is determined by the core structure of the progenitor star. Since $\tau_{\text{adv}} \approx M_{\text{gain}}/\dot{M}$ (cf. Marek & Janka 2009) a larger value of τ_{adv} correlates with a higher mass M_{gain} . Accordingly, the total net heating rate Q_{gain} and thus the heating efficiency $\epsilon \equiv Q_{\text{gain}}/(L_{\nu_e} + L_{\bar{\nu}_e}) = Q_{\text{gain}}/(2L_{\nu})$ of the gas residing in the gain layer is also higher for models that develop an explosion (see Fig. 13 and Murphy & Burrows 2008). Figure 14 shows the ratio of the advection (dwell) timescale to the neutrino-heating timescale in the gain layer (our evaluation employs the Newtonian analog of the formulas given in Müller et al. 2012) for the models also displayed in Figs. 12 and 13. The same trends as in the previous images can be seen. Models closer to an explosion exhibit higher values of the timescale ratio. The ratio approaches unity, indicating the proximity to a runaway instability, roughly around the time when we define the onset of an explosion (i.e., when the average shock radius of Fig. 7 passes 400 km). The quality of the coincidence of these moments, however, differs from model to model and depends on the exact definition used for the timescales and the accuracy at which the relevant quantities can be evaluated in highly perturbed flows. Nevertheless, the evolutionary trend of the timescale ratio (increasing or decreasing) is suggestive for whether a simulation run leads to a successful explosion or failure.

A larger mass in the gain layer and higher total net energy deposition rate are therefore better indicators of the proximity of our models to explosion than the mean entropy of the gas in this region, which does not exhibit the 1D-2D-3D hierarchy with dimension found previously by Nordhaus et al. (2010). As discussed in Sect. 4 the main reason for this discrepancy are most probably the different treatments of neutrino lepton number losses and our consequential recalibration of the energy source terms. This leads to significantly higher energy drain from the cooling layer in our simulations. While this hypothesis is supported by tests that we conducted in 1D, we cannot be absolutely certain that no other effects play a role for the discrepancies between our results and those of Nordhaus et al. (2010), because detailed cross-comparisons are not available and our knowledge of the details of the implementation of neutrino effects by Nordhaus et al. (2010) may be incomplete. Other potential reasons for differences may be connected to the hydrodynamics scheme (PROMETHEUS with a higher-order Godunov solver and directional splitting vs. CASTRO with unsplit methodology, Almgren et al. 2010), the employed grid (polar coordinates vs. structured grid with adaptive refinement by a nested hi-

erarchy of rectangular grids), potentially —though not very likely— the use of a 1D core above $10^{12} \text{ g cm}^{-3}$ in our simulations, or differences in the exact structure and properties of the infall region upstream of the stalled shock as a consequence of different treatments of the collapse phase until 15 ms after core bounce (due to full neutrino transport plus a nuclear-burning approximation in the PROMETHEUS-VERTEX code vs. the simple deleptonization scheme of Liebendörfer 2005) or of different seeding of nonradial hydrodynamic instabilities (in our case by imposed, small random seed perturbations of the density), or linked to differences of the low-density EoS outside of the application regime of the Shen et al. (1998) EoS.

Despite these uncertainties about the exact cause of the differences, whose ultimate elimination will require systematic and time-consuming studies, our results, as they are, send a clear message: The outcome of the 1D-2D-3D comparison and the effects of the third dimension advertised by Nordhaus et al. (2010) “as a key to the neutrino mechanism of core-collapse supernova explosions” are not at all robust results. Instead, the exact slope of the critical explosion condition $L_\nu(\dot{M})$, its location, and its shift with dimension, as well as the existence of a 1D-2D-3D hierarchy of the mass-averaged entropy in the gain layer seem to depend sensitively on subtle details of the neutrino treatment or other numerical aspects of the simulations.

6.2. Resolution dependence

Let us now turn to the second, highly interesting question in connection with our set of models, namely to the resolution dependence of our results. Our set of simulations performed with different angular binnings reveals that quantities that turned out to diagnose healthy conditions for an explosion, i.e. the growth of the average shock radius, the degree of shock deformation, or the mass and total heating in the gain layer (but not the mass-averaged entropy of the matter in the gain region), show a clear dependence on the angular zoning (see Figs. 7, 8, 12, and 13 in contrast to Fig. 4). In particular, 2D models with better angular resolution exhibit more favorable conditions and explode more readily (in agreement with results obtained by Scheck 2007 with a more sophisticated treatment of neutrino transport than the simple heating and cooling source terms applied in our investigation), whereas 3D models obey the opposite behavior. What does the resolution dependence of our simulations tell us about the mechanism leading to explosions in our models? And how can we understand the puzzling finding that 2D and 3D runs follow opposite trends when the angular resolution is refined?

We interpret this as a manifestation of two aspects or facts:

- (1) The success of our models, at least in the neighborhood of the explosion threshold, is fostered mainly by large-scale mass flows as associated with strong SASI activity, but not by enhanced fragmentation of structures and vortex motions on small spatial scales.
- (2) Our resolution study reflects the consequences of the turbulent energy cascade, which redistributes energy fed into the flow by external sources in opposite directions in 2D and 3D: While in 3D the turbulent energy flow goes from large to small scales, it pumps energy from small to large spatial scales in 2D.

Point (1) is supported by the kinetic energies of nonradial mass motions in the gain layer of the 2D and 3D models plot-

ted in Fig. 15. From this picture it is obvious that in the case of successful models the angular kinetic energy is higher and shows an overall trend of growth in time until the blast has taken off. Moreover, the spiky maxima and minima of quasi-periodic variations, which are indicative of the presence of low-order SASI modes, are significantly larger for exploding models. This does not only hold for 2D models, whose lateral kinetic energies exhibit variation amplitudes of several 10% and partially up to even $\sim 50\%$ of the time-averaged value. It is also true for 3D models, although in this case the amplitudes are generally smaller and the nonradial kinetic energy is split essentially equally into lateral and azimuthal contributions. When comparing successful runs in 2D with those in 3D, our studies suggest that in both cases the shock exhibits a growing degree of asphericity (expressed by the standard deviation of the shock deformation plotted in Fig. 8) when the explosion is approached, and the kinetic energy of nonradial mass motions reaches roughly the same magnitude (Fig. 15), at least for models near the explosion threshold.

Actually a variety of observations can be interpreted as support of the hypothesis that flows on the largest possible scales rather than on small scales play a crucial role for the success of the neutrino-heating mechanism in our simulations:

- The strength of low-mode SASI activity in 2D models as indicated by growing fluctuations of the angular kinetic energy and of the shock deformation (Figs. 15, 8) increases with higher resolution in clear correlation with an earlier onset of the explosion (Fig. 7). Stronger SASI activity obviously facilitates explosions, which is visible by a growing average shock radius as well as larger mass and higher total heating rate in the gain layer.
- Exploding models in 2D as well as in 3D exhibit large shock deformation at the time of explosion (although the relative asphericity σ_S/R_S of the shock surface is somewhat smaller in 3D than in 2D; see Figs. 7 and 8).
- More fine structure on small spatial scales, which can be seen in 3D models computed with higher resolution in Figs. 9–11, does not imply improved conditions for an explosion.
- Exploding 2D models are *not* connected with the highest mean entropies in the gain region (Fig. 4). This fuels doubts in a random-walk picture where turbulent vortex motions on small scales enlarge the residence time of matter in the gain layer (Murphy & Burrows 2008) and thus could allow for more energy absorption of such mass elements from neutrinos. If this effect occurred, it does not concern a major fraction of the mass in the gain region.

Point (2) is the only plausible argument we can give for explaining the opposite response to higher angular resolution that we discovered in our 2D and 3D simulations. The sequence of 2D runs with gradually reduced lateral zone sizes reflects the growing violence of large-scale flows by higher fluctuation amplitudes of the kinetic energy in the gain layer (Fig. 15) and larger temporal variations of the average shock radius and shock deformation (Figs. 7, 8). In contrast, more energy on small spatial scales in the 3D case manifests itself by a progressing fragmentation of the flow, leading to a growing richness of vortex structures and finer filaments in the case

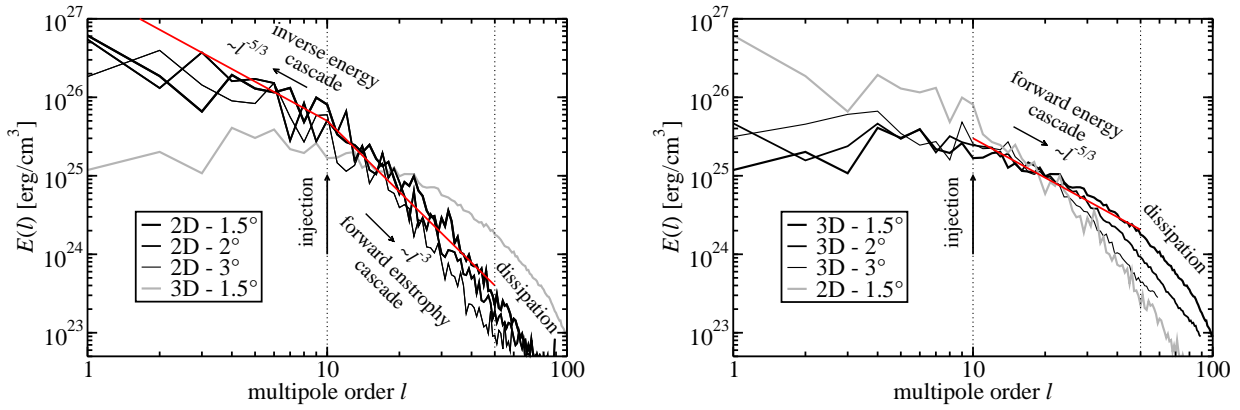


FIG. 16.— Turbulent energy spectra $E(l)$ as functions of the multipole order l for different angular resolution. The spectra are based on a decomposition of the azimuthal velocity v_θ into spherical harmonics at radius $r = 150$ km and 400 ms post-bounce time for $15 M_\odot$ runs with an electron-neutrino luminosity of $L_{\nu_e} = 2.2 \cdot 10^{52}$ erg s $^{-1}$. *Left:* 2D models with different angular resolution (black, different thickness) and, for comparison, the 3D model with the highest employed angular resolution (grey). *Right:* 3D models with different angular resolution and, for comparison, the 2D model with the highest employed angular resolution (grey). The power-law dependence and direction of the energy and enstrophy cascades (see text) are indicated by red lines and labels for 2D in the left panel and 3D in the right panel. The left vertical, dotted line roughly marks the energy-injection scale, and the right vertical, dotted line denotes the onset of dissipation at high l for the best displayed resolution.

of 3D models with smaller angle bins (Figs. 9–11). As a consequence, 3D models with higher angular resolution become more similar to the 1D case in various quantities that we considered as explosion indicators, see, e.g., Figs. 7, 8, 12, and 13.

Both the powerful coherent mass motions of the SASI layer in 2D and the vivid activity in small vortex structures in the 3D environment are fed by two external sources which supply the postshock layer with an inflow of fresh energy: (i) gravitational potential energy that is released by the continuous stream of matter falling through the accretion shock and (ii) energy deposition by neutrinos. The energy stored in the fluid is then redistributed towards small or large scales according to the turbulent cascades characteristic of two- and three-dimensional environments.

Direct evidence for the action of different turbulent energy cascades in 2D and 3D can be obtained by considering the energy spectrum $E(k)$ of turbulent motions as a function of wavenumber k in the gain region. The spectral shape of $E(k)$ can already be adequately established by considering only the azimuthal velocity v_θ at a given radius using a decomposition into spherical harmonics $Y_{lm}(\theta, \phi)$:

$$E(l) = \sum_{m=-l}^l \left| \int_{\Omega} Y_{lm}^*(\theta, \phi) \sqrt{\rho} v_\theta(r, \theta, \phi) d\Omega \right|^2. \quad (8)$$

Here, the velocity fluctuations have been expressed in terms of the multipole order l instead of the wave number k . A summation over the energies of modes with the same l has been carried out⁴, and in order to obtain smoother spectra, we average $E(l)$ over 30 km in radius and over 10 timesteps. One expects that the resulting spectrum $E(l)$ directly reflects the properties of $E(k)$ such as the slopes in different regimes of the turbulent cascade⁵. The computed spectra $E(l)$ (Fig. 16)

⁴ Note that a factor $\sqrt{\rho}$ has been introduced to ensure that the integrated energy of all modes sums up to the total kinetic energy contained in azimuthal motions at radius $r = 150$ km (modulo a normalization factor) (cp. Endeve et al. 2012).

⁵ For the precise relation between Fourier and spherical harmonics power spectra, the reader may consult Chapter 21 of Peebles (1993). For a power-law spectrum $E(k) \propto k^\alpha$, one obtains $E(l) \propto (2l+1)\Gamma(l+\alpha/2+1/2)/\Gamma(l-\alpha/2+3/2)$, or $E(l) \propto l^\alpha$ in the limit of large l . In practice, the power-law indices of $E(l)$ and $E(k)$ appear to correspond well to each other already for

indeed confirm the predictions from 3D and (planar) 2D turbulence theory, at least for sufficiently high multipole order l .

In 3D (right panel), a power-law spectrum with $E(l) \propto l^{-5/3}$ (Landau & Lifshitz 1959) develops at intermediate wavenumbers as the resolution is increased, reflecting the transfer of energy from large to small scales in a forward cascade until dissipation takes over at large l . At high resolution, the energy contained in small-scale disturbances increases, as the dissipation range moves to larger l . One observes that the $5/3$ -power-law is broken at low l ($l \lesssim 10$), suggesting that kinetic energy is injected into the flow at wavenumbers $l \approx 10$, i.e. at scales typical for growing convective plumes.

By contrast, the power-law dependence $E(l) \propto l^{-5/3}$ approximately holds for $l \lesssim 10$ in 2D as a result of the reverse energy cascade (Kraichnan 1967). The energy injected at $l \approx 10$ is therefore not transferred to the dissipative range; only enstrophy (the squared vorticity of the velocity field) is transported in a forward cascade with a different power-law index ($E(l) \propto l^{-3}$).

This appears to be a natural explanation for the predominance of large-scale and small-scale structures in 2D and 3D, respectively. Moreover, this picture suggests that as dissipation affects the “injection scale” at $l \approx 10$ less with increasing resolution, the differences between 2D and 3D become more pronounced with finer grid zoning.

Our analysis of the spectral properties of turbulence thus further strengthens our view that the trends seen in our simulations strongly suggest that nonradial kinetic energy available on large scales, not on small scales, assists the development of an explosion by the neutrino-heating mechanism. This explains why 2D models with higher angular resolution tend to explode earlier and thus at higher values of the mass-accretion rate than less resolved models. On the other hand, the energy “drain” by vortex motions on ever smaller scales—with the same reservoir of pumping energy per unit mass being available from accretion and neutrino heating—disfavors explosions in better resolved 3D models.

We therefore conclude that the key to the mechanism of core-collapse supernova explosions seems intrinsically and tightly linked to the question how much kinetic energy of

$l \gtrsim 4$. Empirically, broken power laws transform in a similar manner.

the matter in the gain region can be accumulated in nonradial fluid motions on the largest possible scales, i.e., in the lowest-order spherical harmonics modes of nonradial hydrodynamic instabilities. The predominant growth of such flows is typical of SASI activity, whose lowest-order spherical harmonics modes possess the highest growth rates (Blondin et al. 2003; Blondin & Mezzacappa 2006b; Foglizzo et al. 2006, 2007; Ohnishi et al. 2006). Strong SASI motions drive shock expansion, increase the gain layer and its mass content, allow a larger fraction of the accreted matter to stay in the gain layer and be exposed to efficient neutrino heating, and thus aid the development of an explosion (Scheck et al. 2008; Marek & Janka 2009). However, our models do not show a systematic trend of higher average entropies of the matter in the gain layer for models closer to explosion. Instead, we find that such models have larger mass, larger nonradial kinetic energy, larger total neutrino-heating rate, and larger total entropy in the gain layer.

7. SUMMARY AND CONCLUSIONS

We have performed a systematic study of the post-bounce evolution of supernova cores of 11.2 and 15 M_{\odot} and their explosion by the neutrino-heating mechanism in 1D, 2D, and 3D, employing simple neutrino cooling and heating terms with varied values of the driving luminosity. We conceptually followed previous studies by Murphy & Burrows (2008) and Nordhaus et al. (2010), but did not apply the deleptonization treatment that they adopted from Liebendörfer (2005), who introduced it for an approximative description of neutrino losses during the infall phase until core bounce. We argued (Sect. 2) that this approximation—with or without the source term proposed by Liebendörfer (2005) to account for entropy generation in neutrino-electron scatterings—does not provide a suitable treatment of the evolution of the electron abundance after core bounce. Therefore we did not consider changes of the net electron fraction Y_e of the stellar plasma at times later than 15 ms after bounce, up to which the collapse was followed with the PROMETHEUS-VERTEX code including full neutrino transport. While ignoring Y_e changes subsequently is certainly not a good approximation, it is not necessarily more unrealistic than describing the lepton-number evolution during the accretion phase of the stalled shock by the scheme of Liebendörfer (2005). As a consequence, we had to replace an exponential factor $e^{-\tau_{\text{eff}}}$, which was introduced in an ad hoc way by Murphy et al. (2009) and Nordhaus et al. (2010) to damp the neutrino source terms at high optical depths τ_{eff} , by $e^{-\tau_{\text{eff}}/2.7}$ in order to reproduce the minimum luminosity found to yield explosions in the 1D simulations by Murphy & Burrows (2008) and Nordhaus et al. (2010). This modification led to enhanced neutrino losses in the cooling layer, which were better compatible with total energy loss rates found in simulations with detailed neutrino transport, e.g., in Buras et al. (2006a), and is responsible for some of the findings and differences discussed in Sect. 4.

Our results and conclusions can be briefly summarized as follows:

1. We cannot reproduce the exact slopes and relative locations of the critical curves $L_{\nu}(\dot{M})$ of 1D, 2D, and 3D simulations found by Nordhaus et al. (2010). While our results confirm the well-known fact that explosions in 2D occur for a lower driving luminosity L_{ν} than in 1D when the mass accretion rate \dot{M} is fixed, we cannot discover any significant further reduction when we go

from 2D to 3D.

2. We cannot confirm that the mass-averaged entropy of the matter in the gain region, $\langle s \rangle$, is a good diagnostic quantity for the proximity to an explosion. As we argued in Sect. 6.1, it is neither clear nor necessary that $\langle s \rangle$ is higher for cases where explosions are obtained more readily. Our successful 2D models do not exhibit larger mean entropies than the corresponding 1D cases, which fail to explode. Instead, we observed that the total mass, total entropy, total neutrino-heating rate, and the nonradial kinetic energy in the gain layer are higher in cases that develop an explosion.
3. We conclude that the tendency for an explosion as a monotonically increasing function of dimension as well as the 1D-2D-3D hierarchy of $\langle s(t) \rangle$ found by Nordhaus et al. (2010) are not robust results. They seem to be sensitive to subtle differences of the approximations of neutrino effects (and/or to other differences in the numerical treatments of the models). It is therefore unclear how far studies with radical simplifications of the neutrino physics (without detailed energy and lepton-number source terms and transport; no feedback between accretion and neutrino properties) can yield results that are finally conclusive for the explosion-triggering processes in real supernova cores.
4. Increasing the angular resolution we observed a clear tendency of 2D models to explode earlier, in agreement with previous results by Scheck (2007), who employed a more sophisticated treatment of neutrino effects based on the transport approximation described in Scheck et al. (2006). In contrast, 3D models show the opposite trend and in a variety of quantities and aspects become more similar to their 1D counterparts. The easier explosion of the 2D models is connected to an enhanced violence of large-scale mass motions in the postshock region due to SASI activity, whereas 3D models with better angular resolution appear to develop less strength in low-order SASI modes.
5. We interpret this finding as a consequence of the opposite turbulent energy cascades in 2D and 3D. In 2D the energy continuously pumped into the gain layer by neutrino heating and the release of gravitational binding energy flows from small to large scales and thus helps to power coherent mass motions on the largest possible spatial scales. In contrast, in 3D this energy seems to instigate flow vorticity and fragmentation of structures on small scales. Evidence for this interpretation is provided by Fig. 16.
6. We also conclude from our resolution studies that the presence of violent mass motions connected to low-order SASI modes is favorable for an explosion (in agreement with arguments given by Marek & Janka 2009 and Scheck et al. 2008). This is supported by the fact that 2D and 3D models that are closer to explosion show signs of growing power in large-scale mass motions (signalled by growing fluctuations of the kinetic energy of nonradial velocity components) and in particular develop significant shock deformation and global ejecta asymmetries when the explosion sets in.

7. We found that higher radial resolution makes explosions more difficult with the setup chosen for the investigated set of models. Higher resolution turned out to prevent explosions or to let them occur later in simulations in 1D, 2D, and 3D. This result could be diagnosed to be a consequence of a local density maximum in the neutrino-cooling layer, which grows with higher resolution and enhances the energy loss by neutrino emission. This density peak, however, is a numerical artifact of the employed simple neutrino-cooling treatment by an analytic source term which is exponentially damped at high densities.

The lack of very precise information on the physics ingredients and their exact implementation, e.g., details of the treatment of neutrino source terms, low-density EoS, and progenitor data when mapped into the simulation and seeded with small random perturbations, as well as a variety of methodical differences like the hydrodynamics scheme, numerical grid, and the use of a 1D core at high densities or not, prevent us from presenting a rigorous proof that could causally link the discrepancies between our results and those of Nordhaus et al. (2010) to one or more well understood reasons. We think that the nagging uncertainties in this context demand a future, involved, collaborative code-comparison project. This will also require considerable amounts of computer time for further 3D simulations, in particular with high resolution, thus needing more computer resources than available to us for the described project.

Despite this deficiency, however, our results suggest that the differences of 3D compared to 2D simulations observed by Nordhaus et al. (2010) are unlikely to be a robust outcome but seem to depend on relevant aspects of the modeling (most probably the neutrino physics but potentially, and not finally excluded, also technical aspects).

We therefore conclude that the influence of 3D effects on the supernova mechanism is presently not clear. We strongly emphasize, however, that the fact that our results do not corroborate improved explosion conditions in 3D compared to 2D *cannot* be used as an argument that 3D effects do not facilitate the supernova explosion mechanism or are of minor importance. We just think that in the context of the neutrino-driven mechanism the relevance and exact role of 3D fluid dynamics are not understood yet. We therefore have the opinion that the results obtained by Nordhaus et al. (2010) do not justify their claims that 3D hydrodynamics offers the key to a fundamental understanding of the neutrino mechanism while other physics in the supernova core, like general relativity or the properties of the nuclear EOS, are only of secondary importance. Though this may well be right, such statements at the present time are premature and not supported by solid facts and results.

Our study, however, raises further important questions. How far can our understanding be developed on grounds of modeling approaches that employ radical simplifications of the neutrino physics? Which aspects of the complex interplay between different components of the problem are linked to the essence of how the explosion is triggered by the combination of neutrino energy supply and nonradial hydrodynamic instabilities? Examples for such mutually dependent components are the neutrino transport and hydrodynamics, the neutron star core evolution and fluid motions around the neutron star, or the mass flux from the accretion shock to the deceleration layer (both being the coupling regions for the advective-

acoustic cycle that is thought to be responsible for the SASI growth; e.g., Scheck et al. 2008) and the conditions in the neutrino heating and cooling layers. Much more work needs to be done to find the answers of these questions.

A major shortcoming of the setup applied in previous works and adopted also in our investigation is the neglect of neutrino cooling and deleptonization inside the proto-neutron star. The employed simple neutrino source terms and their exponential suppression at high optical depths do not allow the neutron star to evolve. Underestimating the neutron star contraction, however, slows down the infall velocities in the postshock layer and thus has unfavorable consequences for the growth of the SASI (Scheck et al. 2008), similar to the effects of reduced neutrino losses in the cooling layer (Scheck et al. 2008) or increased nuclear photodissociation behind the stalled shock (Fernández & Thompson 2009). On the contrary, a slower postshock flow improves the conditions for the growth of convective instability, whose development is supported by a high ratio (larger than ~ 3 signals a linearly unstable situation) of the advection timescale through the gain region divided by the inverse of the Brunt-Väisälä frequency as discussed by Foglizzo et al. (2006), Buras et al. (2006b), and Scheck et al. (2008). It is therefore well possible that the weak SASI activity diagnosed in recent 2D and 3D simulations by Burrows et al. (2012)—leading them to the conclusion that dipolar asymmetries are caused by convection rather than the SASI—is an artifact of the approximative treatment of neutrino cooling and the disregard of neutron star contraction in their models. In full-scale supernova models with sophisticated neutrino transport, Buras et al. (2006b) observed differences in the growth conditions for convection compared to the SASI in collapsing stellar cores of a variety of progenitor stars. Also the high-density equation of state and general relativity, influencing the contraction behavior of the nascent neutron star, can make a difference (Marek & Janka 2009; Müller et al. 2012). Claims, based on highly simplified models, that SASI is less important than convection and at most a minor feature of the supernova dynamics (Burrows et al. 2012) are therefore certainly premature.

Finally, our resolution study suggests that the action of the turbulent cascade in 3D extracts energy from coherent large-scale modes of fluid motion and instead fuels fragmentation and enhanced vortex flows on small spatial scales. At least in our 3D models with better grid zoning the appearance of finer structures in the postshock flow was connected with a tendency of damping the development of explosions. While a finally convincing proof of such a negative feedback may require much better resolved simulations than we presently can afford to conduct (in order to minimize numerical dissipation on small scales), this result implies that good resolution—considerably higher than recently used by Takiwaki et al. (2011), whose 3D simulation had only 32 azimuthal zones (corresponding to a cell size of 11.25°)—is indispensable to clarify the 3D effects on the explosion mechanism. Moreover, our result points to an interesting direction. It is possible that the success of the neutrino-driven mechanism in 3D is tightly coupled to the presence of violent SASI activity, a connection that was found before—and is confirmed by our present study—to foster explosions in 2D? If so, what is the key to instigate such violent SASI motions of the supernova core in three dimensions? Will they occur with a better (more realistic) treatment of the neutrino transport and correspondingly altered conditions in the heating and cooling layers and in the contracting core of the proto-neutron

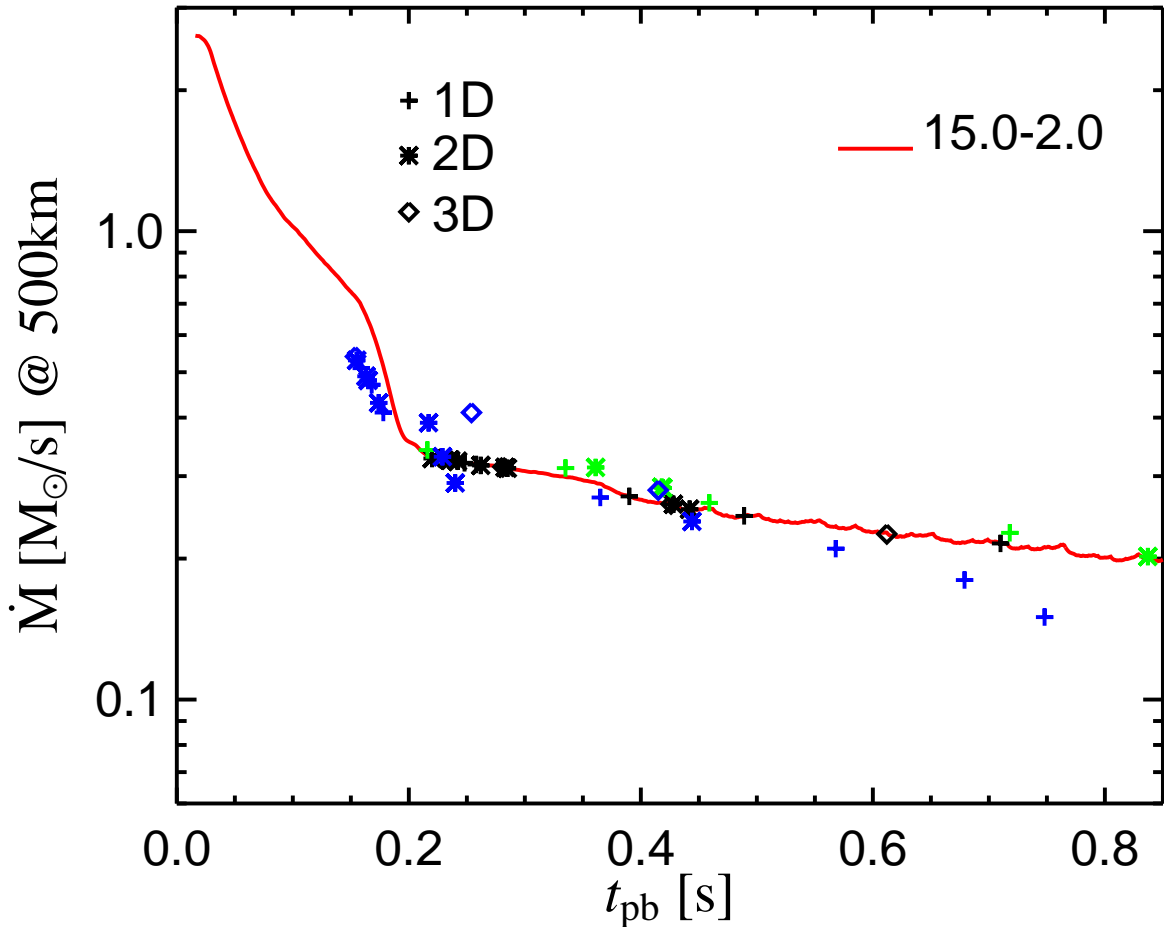


FIG. 17.— Mass accretion rate for the $15 M_{\odot}$ progenitor. The red curve shows the line of Fig. 1. The black symbols represent the values extracted from our simulations at the time t_{exp} when the explosion sets in. Green symbols are data from Murphy & Burrows (2008) and blue symbols those from Nordhaus et al. (2010). Different symbols are used for results of 1D, 2D, and 3D simulations.

star? Or are they associated with stellar rotation, which even with a slow rate can initiate the faster growth of spiral (non-axisymmetric) SASI modes (Blondin & Mezzacappa 2006a; Yamasaki & Foglizzo 2008; Iwakami et al. 2009; Fernández 2010)? Or is strong SASI activity in the supernova core triggered by large-scale inhomogeneities in the three-dimensional progenitor star (Arnett & Meakin 2011), which could provide a more efficient seed for SASI growth than the random cell-to-cell small-amplitude perturbations employed in our simulations? Should the presence of large-amplitude SASI mass motions indeed turn out to be the key to the neutrino mechanism in 3D, it would mean that neutrino-driven explosions are not only a generically multi-dimensional phenomenon, but one that is generically associated with dominant low-order modes of asymmetry and deformation from the very beginning.

While this paper raises many more questions than it is able to answer, it definitely makes clear that our understanding of the supernova physics in the third dimension is still in its very infancy. A virgin territory with distant horizons lies ahead of us and awaits to be explored.

We are grateful to Lorenz Hüpdepohl for his valuable input to different aspects of the reported project and thank Elena Erastova and Markus Rampp (Max-Planck-Rechenzentrum Garching) for their help in the visualization of our 3D data. HTJ would like to thank Rodrigo Fernández, Thierry Foglizzo, Jerome Guilet, and Christian Ott for stimulating and informative discussions. This work was supported by the Deutsche Forschungsgemeinschaft through Sonderforschungsbereich/Transregio 27 “Neutrinos and Beyond”, Sonderforschungsbereich/Transregio 7 “Gravitational-Wave Astronomy”, and the Cluster of Excellence EXC 153 “Origin and Structure of the Universe”. The computations were performed on the Juropa cluster at the John von Neumann Institute for Computing (NIC) in Jülich, partially through a DECI-6 grant of the DEISA initiative, on the IBM p690 at Cineca in Italy through a DECI-5 grant of the DEISA initiative, and on the IBM p690 at the Rechenzentrum Garching.

APPENDIX

A. SIMULATIONS WITH PARAMETRIZED DELEPTONIZATION TREATMENT FOR THE CORE-COLLAPSE PHASE

In this Appendix we briefly report on our efforts to reproduce the 1D results of Murphy & Burrows (2008) and Nordhaus et al. (2010) for the critical explosion conditions of the $15 M_{\odot}$ progenitor, applying a neutrino treatment that was intended to copy the procedure outlined in these publications as closely as possible.

For this purpose we retained the exponential suppression factor $e^{-\tau_{\text{eff}}}$ of Eqs. (4) and (5) without a reduction factor of 2.7 in

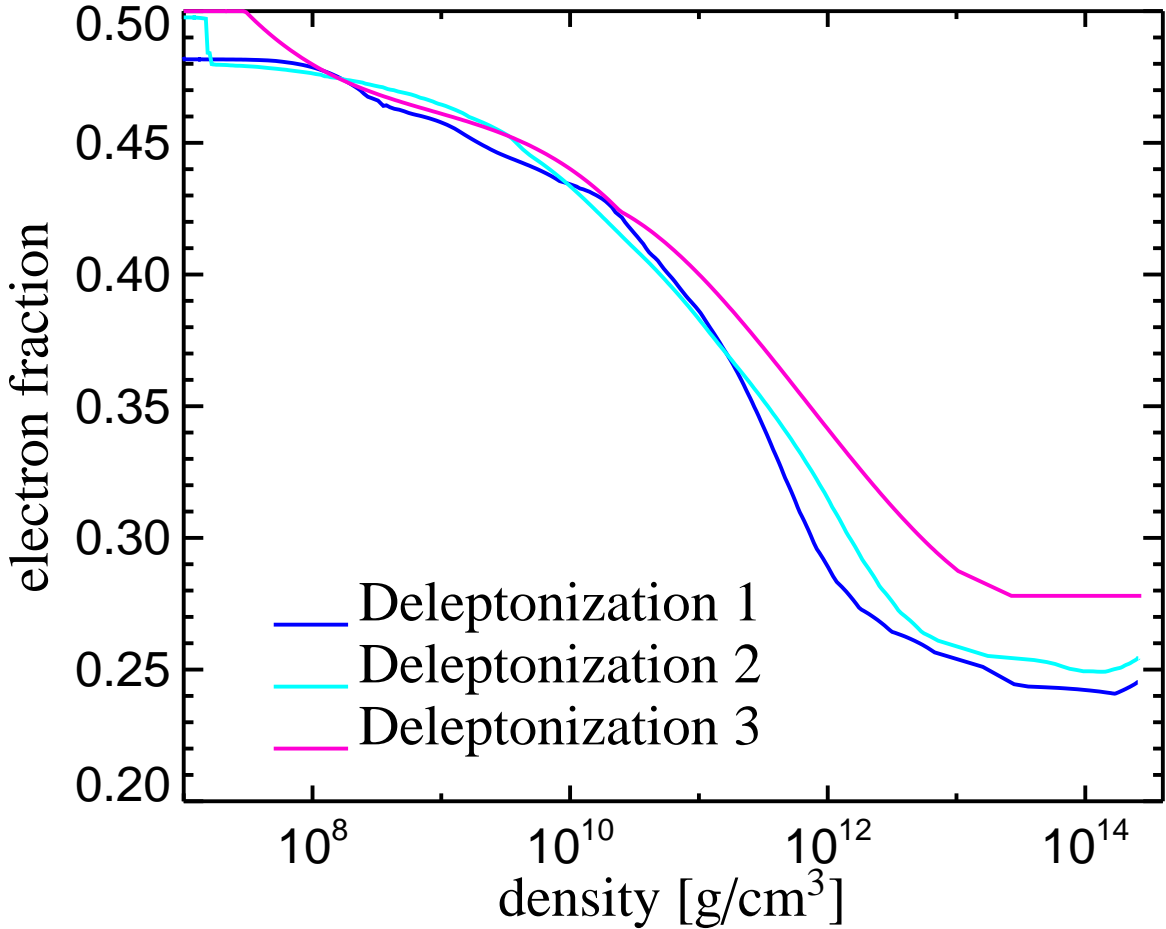


FIG. 18.— Trajectories of the electron fraction with density deduced from different core-collapse studies (see text for details) and employed in our 1D simulations for parametrizing lepton losses by neutrino emission in the stellar core according to Liebendörfer (2005).

the exponent, and the lepton evolution before and after core bounce was described by employing a predefined $Y_e(\rho)$ relation. We also aimed at reproducing the core infall of the previous works as closely as possible, because the density structure of the infall region ahead of the stalled shock determines the mass-infall rate $\dot{M}(t)$ at the shock, and some differences became visible when we compared our values with those given by Murphy & Burrows (2008) and Nordhaus et al. (2010) (Fig. 17). We therefore recomputed the collapse phase from the onset of gravitational instability of the progenitor core through core bounce with the deleptonization scheme of Liebendörfer (2005). Entropy changes were taken into account as suggested by Liebendörfer (2005), but were switched off after core bounce following Murphy & Burrows (2008) and Nordhaus et al. (2010).

We tested three different cases for the functional relation $Y_e(\rho)$: First, we used a tabulated result for the $Y_e(\rho)$ evolution as obtained with the PROMETHEUS-VERTEX code and state-of-the-art electron-capture rates (Langanke et al. 2003) (“Deleptonization 1”). Second, we applied a $Y_e(\rho)$ -table provided by Christian Ott as a co-developer of the CoCoNuT code (<http://www.mpa-garching.mpg.de/hydro/COCONUT/>). These data are based on collapse simulations with the VULCAN/2D code (Livne et al. 2004) (“Deleptonization 2”). Third, we employed a fitting formula given by Liebendörfer (2005) for the parameters of model G15 (“Deleptonization 3”). All three $Y_e(\rho)$ trajectories are depicted in Fig. 18.

The three sets of 1D simulations conducted for this Appendix were performed with 800 radial zones. The corresponding critical luminosity curves $L_{\nu_e}(\dot{M})$ are displayed in Fig. 19 in comparison to those of Murphy & Burrows (2008) and Nordhaus et al. (2010) and to our results of Fig. 2 (for 400 zones, because for this resolution the calibration of the exponential suppression factor for best agreement with the critical curve of Murphy & Burrows (2008) was done). The overall slopes of all three curves are similar but none of them is quantitatively or qualitatively in good agreement with those of Murphy & Burrows (2008) and Nordhaus et al. (2010). Explosions in our simulations occurred significantly more readily (i.e., for lower L_{ν_e}) than in the previous works. This suggests less cooling in our runs, although we made all possible efforts to exactly follow the description of the neutrino treatment in those papers. The steep rise and partly backward bending of our curves for \dot{M} values around $0.2\text{--}0.3 M_{\odot} \text{ s}^{-1}$ can be understood by an inspection of Fig. 20, which shows the time evolution of the shock radius for simulations with prescription “Deleptonization 1” for a selection of neutrino luminosity values. One can see that in the case of $L_{\nu_e} = 2.95 \cdot 10^{52} \text{ erg s}^{-1}$ the shock makes a larger excursion before it returns again. Its reexpansion, leading to an explosion, therefore happens later than in the model with $L_{\nu_e} = 2.7 \cdot 10^{52} \text{ erg s}^{-1}$, where the first shock expansion is much less strong. Correspondingly, the explosion in the former case sets in at a later time and lower mass accretion rate than in the latter case, explaining the backward bending of $L_{\nu_e}(\dot{M})$ in this regime of luminosities and \dot{M} . The nearly horizontal parts of the critical curves can be understood by the fact that for such high values of the luminosities the neutrino cooling (with the unmodified $e^{-\tau_{\text{eff}}}$ suppression factor) is so weak that the

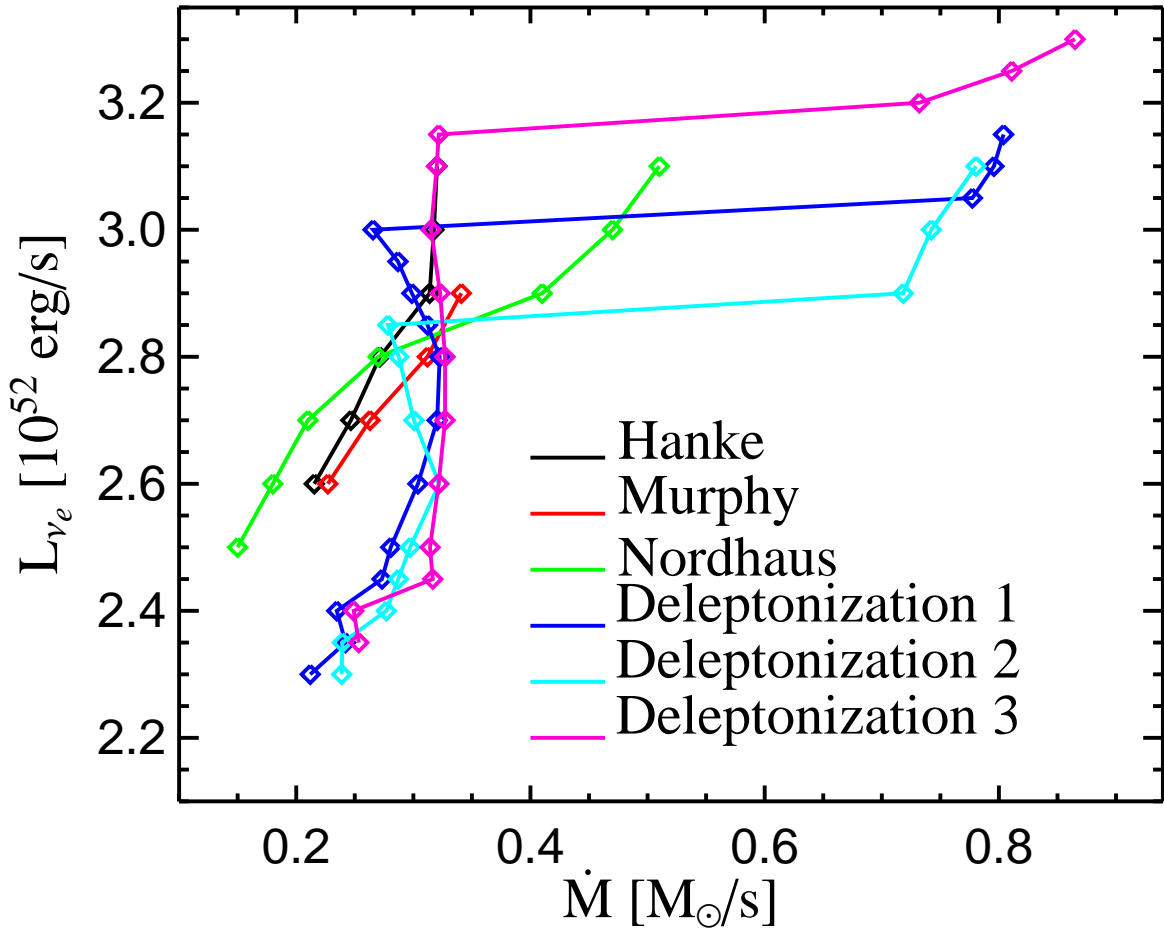


FIG. 19.— Critical curves for the electron-neutrino luminosity (L_{ν_e}) versus mass accretion rate (\dot{M}), representing the explosion threshold for different sets of 1D simulations of the $15 M_{\odot}$ progenitor. The black line corresponds to our results shown as black curve in Fig. 2 (see also Table 1), red are results of Murphy & Burrows (2008), green of Nordhaus et al. (2010), and the three additional curves (dark blue, light blue, and pink) correspond to different sets of simulations that we performed with the deleptonization treatment of Liebendörfer (2005) for the core-collapse phase and the different electron-fraction trajectories of Fig. 18 in our effort to reproduce the 1D results of Murphy & Burrows (2008) and Nordhaus et al. (2010).

explosion sets in very early (see the black line in Fig. 20) and therefore for large values of the mass accretion rate. The region between $\dot{M} \approx 0.3 M_{\odot} s^{-3}$ and $\dot{M} \approx 0.8 M_{\odot} s^{-3}$ is difficult to probe with a stepwise increase of L_{ν_e} , because the mass-accretion rate there changes so rapidly that the shock shows time-dependent dynamics instead of settling into a quasi-steady state.

None of the critical curves obtained with the direct implementation of the neutrino treatment described in Murphy & Burrows (2008) and Nordhaus et al. (2010) can reproduce the critical luminosity curves reported in these papers reasonably well. We therefore decided to proceed with the modifications described in Sect. 2.

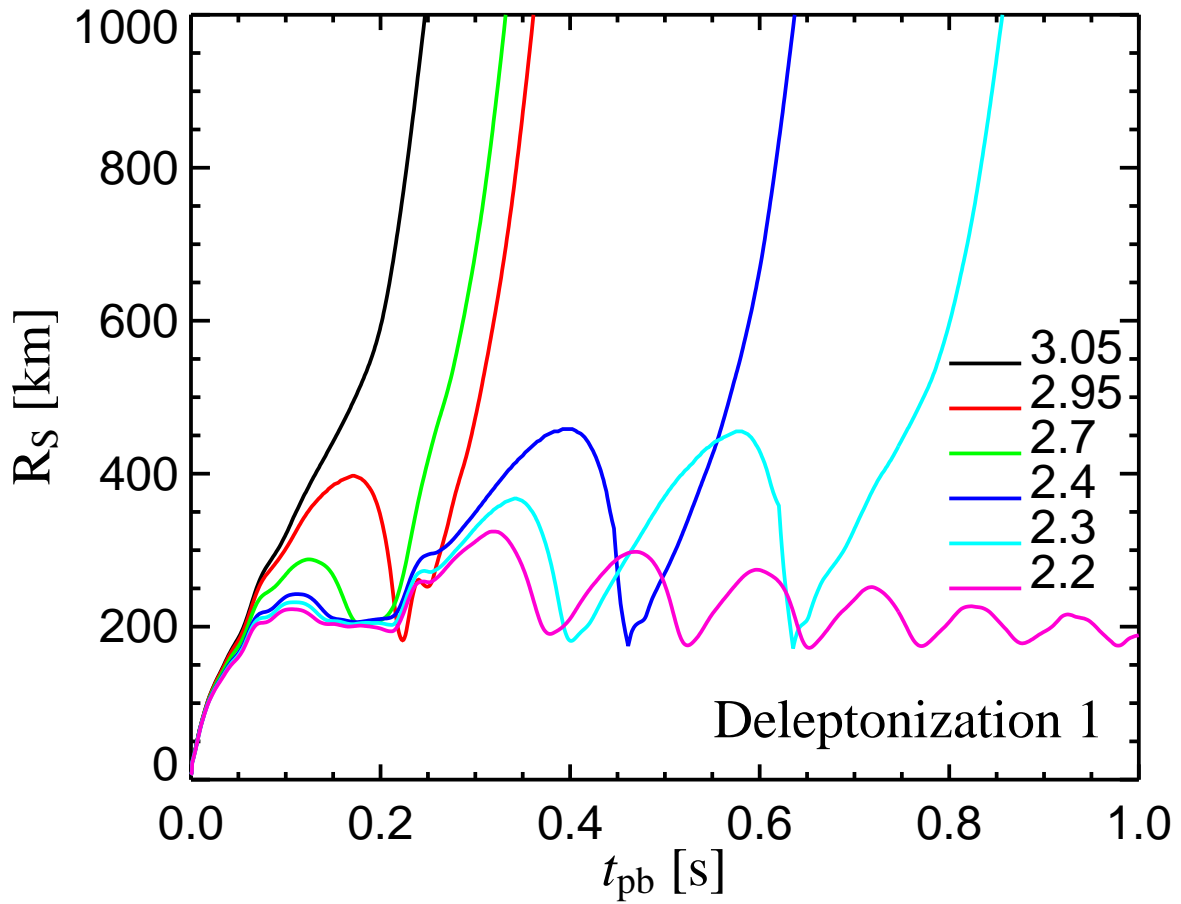


FIG. 20.— Time evolution of the shock radius as a function of post-bounce time, t_{pb} , for 1D simulations performed with the deleptonization scheme of Liebendörfer (2005) for electron-fraction trajectory “Deleptonization 1” of Fig. 18. The colors correspond to different electron-neutrino luminosities, which are labeled in the plot in units of $10^{52} \text{ erg s}^{-1}$.

REFERENCES

- Almgren, A. S., Beckner, V. E., Bell, J. B., et al. 2010, *ApJ*, 715, 1221
- Arnett, W. D. & Meakin, C. 2011, *ApJ*, 733, 78
- Blondin, J. M., Mezzacappa, A., & DeMarino, C. 2003, *ApJ*, 584, 971
- Blondin, J. M. & Mezzacappa, A. 2006a, *Nature*, 445, 58
- Blondin, J. M. & Mezzacappa, A. 2006b, *ApJ*, 642, 401
- Bruenn, S. W., Mezzacappa, A., Hix, W. R., et al. 2009, in *American Institute of Physics Conference Series*, Vol. 1111, American Institute of Physics Conference Series, ed. G. Giobbi, A. Tornambe, G. Raimondo, M. Limongi, L. A. Antonelli, N. Menci, & E. Brocato, 593–601
- Buras, R., Rampp, M., Janka, H.-T., & Kifonidis, K. 2006a, *A&A*, 447, 1049
- Buras, R., Janka, H.-T., Rampp, M., & Kifonidis, K. 2006b, *A&A*, 457, 281
- Burrows, A., & Goshy, J. 1993, *ApJ*, 416, L75
- Burrows, A., Dolenca, J. C., & Murphy, J. W. 2012, submitted to *ApJ*, ArXiv e-prints 1204.3088
- Burrows, A., Hayes, J., & Fryxell, B. A. 1995, *ApJ*, 450, 830
- Burrows, A., Livne, E., Dessart, L., Ott, C. D., & Murphy, J. 2006, *ApJ*, 640, 878
- Burrows, A., Livne, E., Dessart, L., Ott, C. D., & Murphy, J. 2007, *ApJ*, 655, 416
- Colella, P. & Glaz, H. M. 1985, *J. Comput. Phys.*, 59, 264
- Colella, P. & Woodward, P. R. 1984, *J. Comput. Phys.*, 54, 174
- Einfeldt, B. 1988, *SIAM Jour. Numer. Anal.*, 25, 294
- Endeve, E., Cardall, C. Y., Budiardja, R. D., et al. 2012, ArXiv e-prints 1203.3108
- Fernández, R. 2010, *ApJ*, 725, 1563
- Fernández, R. 2012, *ApJ*, 749, 142
- Fernández, R. & Thompson, C. 2009, *ApJ*, 697, 1827
- Foglizzo, T., Scheck, L., & Janka, H. Th. 2006, *ApJ*, 652, 1436
- Foglizzo, T., Galletti, P., Scheck, L., & Janka, H. Th. 2007, *ApJ*, 654, 1006
- Fryxell, B., Müller, E., & Arnett, D. 1991, *ApJ*, 367, 619
- Herant, M., Benz, W., Hix, W. R., Fryer, C. L., & Colgate, S. A. 1994, *ApJ*, 435, 339
- Iwakami, W., Kotake, K., Ohnishi, N., Yamada, S., & Sawada, K. 2008, *ApJ*, 678, 1207
- Iwakami, W., Kotake, K., Ohnishi, N., Yamada, S., & Sawada, K. 2009, *ApJ*, 700, 232
- Janka, H.-T. 2001, *A&A*, 368, 527
- Janka, H.-T. & Müller, E. 1996, *A&A*, 306, 167
- Kraichnan, R. H. 1967, *Physics of Fluids*, 10, 1417
- Landau, L.D. & Lifshitz, E.M. 1959, *Course of Theoretical Physics, Fluid Mechanics*, Vol. 6 (Reading, MA: Addison-Wesley)
- Langanke, K., Martínez-Pinedo, G., Sampaio, J. M., et al. 2003, *Physical Review Letters*, 90, 241102
- Liebendörfer, M. 2005, *ApJ*, 633, 1042
- Livne, E., Burrows, A., Walder, R., Lichtenstadt, I., & Thompson, T. A. 2004, *ApJ*, 609, 277
- Marek, A. & Janka, H.-T. 2009, *ApJ*, 694, 664
- Müller, B., Janka, H.-T., & Marek, A. 2012, submitted to *ApJ*, ArXiv e-prints 1202.0815
- Müller, E., Fryxell, B., & Arnett, D. 1991a, *A&A*, 251, 505
- Müller, E., Fryxell, B., & Arnett, D. 1991b, in *European Southern Observatory Conference and Workshop Proceedings*, Vol. 37, ed. I. J. Danziger & K. Kjaer, 99
- Murphy, J. W. & Burrows, A. 2008, *ApJ*, 688, 1159
- Murphy, J. W., Ott, C. D., & Burrows, A. 2009, *ApJ*, 707, 1173
- Nordhaus, J., Burrows, A., Almgren, A., & Bell, J. 2010a, *ApJ*, 720, 694
- Ohnishi, N., Kotake, K., & Yamada, S. 2006, *ApJ*, 641, 1018
- Peebles, P. J. E. 1993, *Principles of Physical Cosmology*, Princeton, NJ: Princeton University Press
- Pejcha, O. & Thompson, T. A. 2011, *ApJ*, 746, 106
- Plewa, T. & Müller, E. 1999, *A&A*, 342, 179
- Quirk, J. J. 1994, *Int. J. Num. Meth. Fluids*, 18, 555
- Rampp, M. & Janka, H.-T. 2002, *Astron. Astrophys.*, 396, 361
- Sato, J., Foglizzo, T., & Fromang, S. 2009, *ApJ*, 694, 833
- Scheck, L. 2007, PhD thesis, Technical University Munich
- Scheck, L., Kifonidis, K., Janka, H.-Th., & Müller, E. 2006, *A&A*, 457, 963
- Scheck, L., Janka, H.-Th., Foglizzo, T., & Kifonidis, K. 2008, *A&A*, 477, 931
- Shen, H., Toki, H., Oyamatsu, K., & Sumiyoshi, K. 1998, *Nuclear Physics A*, 637, 435
- Strang, G. 1968, *SIAM J. Numer. Anal.*, 5, 506
- Suwa, Y., Kotake, K., Takiwaki, T., et al. 2010, *PASJ*, 62, L49+
- Takiwaki, T., Kotake, K., & Suwa, Y. 2011, *ApJ*, 749, 98
- Thielemann, F.-K., Hirschi, R., Liebendörfer, M., & Diehl, R. 2011, in *Lecture Notes in Physics*, Berlin Springer Verlag, Vol. 812, Lecture Notes in Physics, Berlin Springer Verlag, ed. R. Diehl, D. H. Hartmann, & N. Prantzos, 153–232
- Woosley, S. E., Heger, A., & Weaver, T. A. 2002, *Reviews of Modern Physics*, 74, 1015
- Woosley, S. E., & Weaver, T. A. 1995, *ApJS*, 101, 181
- Yamasaki, T. & Foglizzo, T. 2008, *ApJ*, 679, 607
- Yamasaki, T. & Yamada, S. 2005, *ApJ*, 623, 1000
- Yamasaki, T. & Yamada, S. 2006, *ApJ*, 650, 291